

# Density-controlled metalloporphyrin with mutated surface via pulsed laser for oxidative refining of alcohols to benzoic acid and H<sub>2</sub> production using linear tandem electrolysis

Talshyn Begildayeva <sup>a,1</sup>, Jayaraman Theerthagiri <sup>a,1</sup>, Ahreum Min <sup>b,1</sup>, Cheol Joo Moon <sup>b,1</sup>, Myong Yong Choi <sup>a,b,\*</sup>

<sup>a</sup> Department of Chemistry (BK21 FOUR), Research Institute of Natural Sciences, Gyeongsang National University, Jinju 52828, Republic of Korea

<sup>b</sup> Core-Facility Center for Photochemistry & Nanomaterials, Gyeongsang National University, Jinju 52828, Republic of Korea

## ARTICLE INFO

### Keywords:

Pulsed laser ablation in liquids  
Ni<sub>3</sub>S<sub>2</sub>  
Nickel tetraphenylporphyrin  
Benzyl alcohol oxidation  
H<sub>2</sub> fuel generation  
Benzoic acid production  
Tandem water electrolysis

## ABSTRACT

A highly selective and multifunctional electrocatalyst is constructed by combining a single-phase Ni<sub>3</sub>S<sub>2</sub> obtained via pulsed laser ablation in liquids (PLAL) with different contents of nickel tetraphenylporphyrin (NiTPP) complex. The catalytic performance is assessed in consecutive hydrogen (HER) and oxygen evolution (OER), as well as benzyl alcohol (B.Alc) oxidation reactions (AOR). The optimal NiS-NiTPP10% exhibits the highest activity with overpotentials of 435, 320, and 170 mV, respectively. Moreover, NiS-NiTPP10% favors alcohol oxidation reaction and produces benzoic acid (B.Ac) at a yield rate of 2.23 mM h<sup>-1</sup> cm<sup>-2</sup> with 100% mass balance, 98.3% Faradaic efficiency (FE), and 99.8% selectivity. Finally, the system with simultaneous H<sub>2</sub> evolution and value-added B.Ac production is successfully employed in a NiS-NiTPP10%||NiS-NiTPP10% electrolyzer, resulting in a high FE of 81% and 99%, and a yield rate of 0.42 and 4.03 mM h<sup>-1</sup> cm<sup>-2</sup>, respectively, at a lower cell voltage of 193 mV than the standard water electrolyzer. The pyrrole rings of NiTPP could act as the terminal for the B.Alc molecule, and the Ni<sup>2+</sup>/Ni<sup>3+</sup> redox pair of Ni<sub>3</sub>S<sub>2</sub> could accelerate the oxidation process. Hence, both Ni<sub>3</sub>S<sub>2</sub> and NiTPP boost the performance of NiS-NiTPP10% via charge-density modulation and strong synergistic effects.

## 1. Introduction

The current global energy crisis underscores the urgent need for the development of innovative and multifunctional materials that can efficiently generate value-added chemicals and energy-saving H<sub>2</sub> fuel via water electrolysis [1–4]. The transformation of primary alcohols, such as benzyl alcohol (B.Alc), into valuable compounds, including benzoic acid (B.Ac) or benzaldehyde (B.Ald) via selective electrooxidation, is gaining traction. This method is particularly appealing as it offers a more efficient alternative to the kinetically sluggish electrochemical oxygen evolution reaction (OER) in water electrolyzers. This efficiency is due to the relatively low oxidation potential of B.Alc, which facilitates a more favorable reaction pathway [5–7]. However, improving the selectivity of B.Ac is essential due to its importance in the pharmaceutical, food, and chemical industries [8–12]. Various attempts have been made to

enhance selectivity, including the use of noble metals, single-phase materials, and heterostructures [13–25]. However, the scarcity of noble metals and low selectivity hinder scaling up. Composites that mimic natural systems, such as metalloporphyrins, are crucial and interesting from both scientific and practical perspectives. In addition to their biological importance in oxygen transport, metalloporphyrins have been investigated for applications in catalysis, sensing, and electrochemistry. Some metalloporphyrins, such as iron porphyrins, are effective electrocatalysts for the ORR, which is important in fuel cells and other electrochemical devices [26,27]. Metalloporphyrins, such as cobalt and nickel porphyrins, have been examined as catalysts for the hydrogen evolution reaction (HER) [28–30]. In addition to these applications, metalloporphyrins have been investigated as electrocatalysts for other important reactions, including carbon dioxide reduction and OER [31–34]. These composites successfully drive many other

\* Corresponding author at: Department of Chemistry (BK21 FOUR), Research Institute of Natural Sciences, Gyeongsang National University, Jinju 52828, Republic of Korea.

E-mail address: [mychoi@gnu.ac.kr](mailto:mychoi@gnu.ac.kr) (M.Y. Choi).

<sup>1</sup> These authors contributed equally to this work



electrochemical reactions owing to their unique electronic and structural properties, making them attractive as ready-to-tune electrocatalysts. Unfortunately, the durability of bare metalloporphyrin is inadequate during continuous reactions under harsh alkaline conditions. To overcome this challenge, metalloporphyrin is combined with other electrochemically active materials, such as nickel sulfides ( $\text{Ni}_x\text{S}_y$ ).

$\text{Ni}_x\text{S}_y$  is a well-known electrocatalyst for various electrochemical reactions, including the electrooxidation of organic compounds, such as B.Alc [35].  $\text{Ni}_x\text{S}_y$  can deliver a more surface area and active sites for the electrooxidation of B.Alc and facilitate the electron transfer from the B.Alc to the electrode, promoting the reaction by reducing the activation energy of the process. Most importantly, it can enhance electrode stability during electrochemical reactions [36]. The high stability and durability of  $\text{Ni}_x\text{S}_y$  nanoparticles (NPs) can prevent electrode deactivation during the reaction, leading to efficient and selective electrocatalytic performance.  $\text{Ni}_x\text{S}_y$  and nickel tetraphenylporphyrin (NiTPP) are different materials with distinct properties, and possible synergy could exist in B.Alc oxidation (AOR).

Solvothermal and wet-chemical approaches are generally widespread methods for synthesizing  $\text{Ni}_x\text{S}_y$  and NiTPP. However,  $\text{Ni}_x\text{S}_y$  could be obtained in a more eco-friendly and facile manner compared to those methods. Pulse laser ablation in liquid (PLAL) is recognized as a green and uncomplicated technique for the synthesis of  $\text{Ni}_x\text{S}_y$  NPs. This method necessitates only a nickel metal plate and a source of sulfur [37–41]. It is particularly advantageous for the fabrication of electrocatalysts with pristine surfaces and accessible active sites, as the use of surfactants or reducing agents to facilitate material formation is not required. Consequently, materials synthesized under the highly non-equilibrium conditions of the PLAL process exhibit superior performance in catalytic, photocatalytic, and electrochemical applications compared to those prepared via traditional methods [42–50].

Herein, PLAL-synthesized single-phase  $\text{Ni}_3\text{S}_2$  was ultrasonically combined with 5 wt%, 10 wt%, and 15 wt% of NiTPP metal-organic complex. To the best of our knowledge, this system was successfully used as an electrocatalyst in a hybrid electrolyzer (HER||AOR) for the energy-saving and selective generation of  $\text{H}_2$  fuel and value-added B.Ac for the first time. Composites outperform the bare  $\text{Ni}_3\text{S}_2$  and NiTPP in HER with the lowest overpotential ( $\eta$ ) of 435 mV at 10 mA cm<sup>-2</sup> with a mass activity of 427.6 mA mg<sup>-1</sup> EC<sub>CSA</sub> owing to its improved charge transfer kinetics. Moreover, NiS-NiTPP efficiently drives the AOR, and optimized NiS-NiTPP10% yields the highest rate of B.Ac production of 2.23 mM h<sup>-1</sup> cm<sup>-2</sup> with a high mass balance, FE and selectivity of 100%, 98.3%, and 99.8% at 1.45 V vs. RHE, respectively. Finally, the symmetric (NiS-NiTPP10%||NiS-NiTPP10%) hybrid electrolyzer affords an  $\text{H}_2$  gas yield rate of 0.42 mM h<sup>-1</sup> cm<sup>-2</sup> with a FE of 81% at a lower cell voltage of 193 mV than the standard water electrolyzer. It simultaneously produces value-added B.Ac in the anodic compartment with a yield rate of 4.03 mM h<sup>-1</sup> cm<sup>-2</sup> and a FE of 99%.

## 2. Experimental

### 2.1. Synthesis of electrocatalysts

#### 2.1.1. Preparation of NiTPP

NiTPP was produced via a solvothermal process. Briefly, 100 mg of  $\text{NiCl}_2 \cdot 6 \text{H}_2\text{O}$  and 78 mg of TPP were dissolved in 25 mL of DMF and 5 mL of methanol under constant stirring. Then, the reaction solution was relocated to a Teflon reactor chamber and kept at 130 °C for 24 h. The obtained metal-organic complex material was thoroughly washed many times with methanol, centrifuged at 10000 rpm for 10 min to get precipitate, and dried in an oven at 50 °C overnight. Dried NiTPP powder was used for further characterization.

#### 2.1.2. Synthesis of single-phase $\text{Ni}_3\text{S}_2$

A neodymium-doped yttrium aluminum garnet pulsed laser (repetition rate = 10 Hz and pulse width = 7 ns) of 1064 nm wavelength and

100 mJ pulse power was focused on a nickel plate surface immersed in 10 mL of 50 mM thioacetamide aqueous solution with a focusing lens ( $f = 30$  mm). Ablation was achieved in 20 min under constant stirring. After PLAL, colloidal solutions of single-phase  $\text{Ni}_3\text{S}_2$  were washed several times with water, collected via centrifugation at 14000 rpm for 10 min, and oven-dried at 50 °C overnight.

#### 2.1.3. Synthesis of NiS-NiTPP (5 wt%, 10 wt%, and 15 wt%)

Dried  $\text{Ni}_3\text{S}_2$  and calculated amounts of NiTPP were dispersed in absolute methanol and treated ultrasonically for 30 min to homogenize single-phase  $\text{Ni}_3\text{S}_2$  NP dispersion on the NiTPP microstructures. Next, samples were rinsed with absolute methanol and centrifuged at 14000 rpm for 10 min. Composites were kept in an oven at 50 °C overnight and marked as NiS-NiTPP5%, NiS-NiTPP10%, and NiS-NiTPP15%.

### 2.2. Quantitative analysis of AOR products in liquid phase via HPLC

The B.Alc conversion to the consistent B.Ac and B.Ald was monitored via the YL9100 HPLC system with a UV-vis detector (YOUNGIN Chromass) and a 4.6 mm × 50 mm, 1.8 μm C18 column (Agilent SB-C18). During 1 h of AOR, 50 μL of the anolyte was taken out every 15 min, diluted with 1 mL of DI water, and the absorbance of the reaction mixture was measured at 245 nm. 0.02 M aqueous solution of formic acid to acetonitrile ratio of 70:30 was used as the eluent and ran at 0.3 mL min<sup>-1</sup> flow rate in the isocratic mode for 12 min. Calibration curves obtained from a known concentration of B.Alc, B.Ald, and B.Ac (1, 2, 5, and 10 mM) were used to quantify the amount of reactant conversion to the corresponding product during AOR. Reaction parameters, such as B.Alc conversion, mass balance, selectivity toward B.Ac and B.Ald and FE were calculated from the following formulas (1–5), respectively:

$$\text{B.Alc conversion } (\%) = \frac{C(\text{B.Alc})_t}{C(\text{B.Alc})_0} * 100\% \quad (1)$$

$$\text{Mass balance } (\%) = \frac{C(\text{B.Alc})_t + C(\text{B.Ac})_t + C(\text{B.Ald})_t}{C(\text{B.Alc})_0} * 100\%, \quad (2)$$

$$\text{Selectivity (B.Ac)} = \frac{C(\text{B.Ac})_t}{C(\text{B.Alc})_0 - C(\text{B.Alc})_t} * 100\%, \quad (3)$$

$$\text{Selectivity (B.Ald)} = \frac{C(\text{B.Ald})_t}{C(\text{B.Alc})_0 - C(\text{B.Alc})_t} * 100\%, \quad (4)$$

$$\text{Faradaic efficiency (FE)(B.Ac)} = \frac{4 * C(\text{B.Ac})_t * F}{Q} * 100\%, \quad (5)$$

where  $C(\text{B.Alc})_0$  and  $C(\text{B.Alc})_t$  denote the B.Alc concentration at the beginning and a given time in 50 mL of anolyte (mM);  $C(\text{B.Ac})_t$  and  $C(\text{B.Ald})_t$  indicate the concentration of produced B.Ac and B.Ald in 50 mL of anolyte at a given time, respectively (mM), Q is the total number of charge, and 4 is the number of electrons involved in AOR.

### 2.3. Quantitative analysis of $\text{H}_2$ gas using gas chromatography

$\text{H}_2$  gas evolution in the cathode compartment was monitored every 20 min during 2 h of electrolysis at a constant cell voltage in a sealed symmetric hybrid H-cell using gas chromatography (DANI MASTER GC) with  $\text{N}_2$  as the carrier gas. The produced volume of  $\text{H}_2$  gas was estimated from the calibration curve based on the measurements of known volumes of the standard  $\text{H}_2$  gas of high purity (50, 100, 150, 200, and 250 μL). The FE of  $\text{H}_2$  evolution was calculated from the following formula (6):

$$\text{Faradaic efficiency (FE)(H}_2) = \frac{2 * C(\text{H}_2)_t * F}{Q} * 100\%, \quad (6)$$

where 2 is the electron numbers involved in the half-cell HER and  $C(H_2)$  denotes the volume of  $H_2$  at a given time ( $\mu\text{L}$ ).

### 3. Results and discussion

#### 3.1. Structural analyses

A schematic representation of the synthesis pathway for NiTPP5%, 10%, and 15% is presented in [Scheme S1](#). The NiTPP complex was prepared via a solvothermal process, and single-phase  $\text{Ni}_3\text{S}_2$  NPs were obtained using PLAL. Next, the calculated amount of  $\text{Ni}_3\text{S}_2$  NPs and NiTPP complex was mixed in methanol and ultrasonically treated to give a fine dispersion and facilitate strong interaction of single-phase  $\text{Ni}_3\text{S}_2$  NPs on the NiTPP microstructures.

The Ni-ion insertion on the central position of the TPP planar molecule and the formation of a metal–carbon bond was confirmed using UV–vis spectroscopy and XRD analysis ([Figure S1](#)). The porphyrin metalation can generally represent  $\text{Ni}^{2+} + \text{H}_2\text{P} \rightarrow \text{PM} + 2\text{H}^+$ , where  $\text{H}_2\text{P}$  stands for the neutral porphyrin with two protons attached to the nitrogen atoms. The UV–vis absorbance spectrum of a typical TPP has two distinctive features: a strong transition to the second excited state ( $S_0 \rightarrow S_2$ ) at  $\sim 400$  nm (i.e., Soret band) and a weak transition to the first excited state ( $S_0 \rightarrow S_1$ ) at 500–700 nm range (the Q band) ([Figure S1a](#)), which are arising from  $\pi-\pi^*$  transitions [51,52]. Upon metalation, the UV–vis spectrum of neutral TPP showed low-intense Q bands with  $\lambda_{\text{max}} = 526$  nm for NiTPP, mainly owing to the increased symmetry of the molecule [53]. Accordingly, the XRD pattern of TPP underwent some changes after metalation, confirming a successful Ni-ion insertion into the TPP molecule ([Figure S1b](#)). The results of XRD, Raman, and FTIR for  $\text{Ni}_3\text{S}_2$ , NiTPP, and NiS-NiTPP5%, 10%, and 15% are presented in [Fig. 1a, b, and c](#), respectively.

The XRD pattern of single-phase  $\text{Ni}_3\text{S}_2$  contains peaks corresponding to the pure  $\text{Ni}_3\text{S}_2$  (JCPDS card no. 04–1418) phase; all peak positions and relative intensities perfectly match those reported in previous works [54–56]. NiTPP complex exhibits sharp and intense peaks in the 20 range of 5°–30°, confirming the highly crystalline nature of metal–organic complex, and the peak locations and comparative intensities agree with the reported values for metalloporphyrins [57,58]. NiS-NiTPP5%, 10%, and 15% composites demonstrate distinct peaks of  $\text{Ni}_3\text{S}_2$ , along with sharp peaks of NiTPP. The intensity of these peaks upsurges with the amount of NiTPP in the single-phase  $\text{Ni}_3\text{S}_2$ , which confirms the interaction between the two components ([Fig. 1a](#)). Next, all composites were examined using Raman spectroscopy, and the ensuing spectra are presented in [Fig. 1b](#).  $\text{Ni}_3\text{S}_2$  has characteristic sharp Raman active modes in the 200–400  $\text{cm}^{-1}$  range, corresponding to the

heazlewoodite phase [54]. NiTPP spectrum is manifold owing to its complex macrocyclic structure composed of four pyrrole subunits linked via methine bridges. With this, only the most prominent and characteristic modes of metalloporphyrin complexes at 403.47  $\text{cm}^{-1}$  ( $\nu(\text{M}-\text{N})$ ), 1005.05 and 1016.09  $\text{cm}^{-1}$  ( $\nu(\text{pyrrole breathing})$  and phenyl), 1081.33  $\text{cm}^{-1}$  ( $\delta(\text{C}_\beta-\text{H})$ ), 1228  $\text{cm}^{-1}$  ( $\nu(\text{C}_\text{m}-\text{Ph})$ ), and 1371.2  $\text{cm}^{-1}$  ( $\nu(\text{C}_\alpha-\text{N})/\nu(\text{C}_\alpha\text{C}_\beta)$ ) are highlighted, which are in accordance with the reported values [59]. These modes further confirm the successful metalation of planar TPP via Ni-ion insertion into the center of the molecule. As the weight percentage of NiTPP rises from 5 wt% to 15 wt%, the prominent Raman modes of  $\text{Ni}_3\text{S}_2$  and NiTPP become highly visible in the composites, indicating a thorough interosculating and stability of counterparts after ultrasonic treatment ([Fig. 1b](#)).

FTIR spectra are further recorded, the most prominent characteristic bands of  $\text{Ni}_3\text{S}_2$  and NiTPP in the composite materials broaden and intensity gradually increases from NiS-NiTPP5% to NiS-NiTPP15%, such as  $\text{Ni}_3\text{S}_2$  peaks observed at  $\sim 1000$   $\text{cm}^{-1}$  (bending vibration of sulfide groups bounded to Ni ions) and NiTPP bands observed at 750–800  $\text{cm}^{-1}$  (out-of-plane bending of benzene skeletal stretching), 1200–1300  $\text{cm}^{-1}$  (in-plane bending), and 1000–1100  $\text{cm}^{-1}$  (metalloporphyrin skeletal ring). Following sonication, new bands indicative of metal–sulfur bonding emerges around 600  $\text{cm}^{-1}$ , along with the symmetric stretching vibration of pyrroles at 1650  $\text{cm}^{-1}$  [60,61]. These bands progressively intensify from NiS-NiTPP5% to NiS-NiTPP15%, signifying the formation of a proper bond between  $\text{Ni}_3\text{S}_2$  and the Ni center in NiTPP. Consequently, this interaction destabilizes the porphyrin matrix ([Fig. 1c](#)) [59,60,62–64]. This strong bond formation between  $\text{Ni}_3\text{S}_2$  and NiTPP is governed by a similar mechanism to that observed in strong metal–support interactions, wherein the deposition of metallic NPs on the surface of a substrate, such as reducible oxides, forms a strong bond between the metal centers of the deposited NPs and the metal sites of the substrate. This results in orbital overlap and significant charge transfer [65–67]. This rationale is somewhat applicable to the  $\text{Ni}_3\text{S}_2$  and NiTPP system, where  $\text{Ni}_3\text{S}_2$  acts as dispersed metal NPs (exhibiting a metallic nature with a very narrow bandgap) on the conductive substrate (NiTPP, which generally enhances electron transfer). Thus, the interaction between metal sites in  $\text{Ni}_3\text{S}_2$  and NiTPP is poised to effectively yield NiS-NiTPP composites with customized catalytic properties. Consequently, this strong interaction influences the intensity of the Ni–S bond in the FTIR spectra of NiS-NiTPP, which notably increases with the loading wt% of NiTPP in the composite [68,69]. The XPS survey was recorded for bare  $\text{Ni}_3\text{S}_2$ , NiTPP, and optimized NiS-NiTPP10%, as exposed in [Figure S2](#). The survey spectrum of NiS-NiTPP10% composite contains signals from both bare materials, i.e., S 2p signal originated from  $\text{Ni}_3\text{S}_2$  and N 1 s peak owing to the 10 wt% NiTPP in composition.

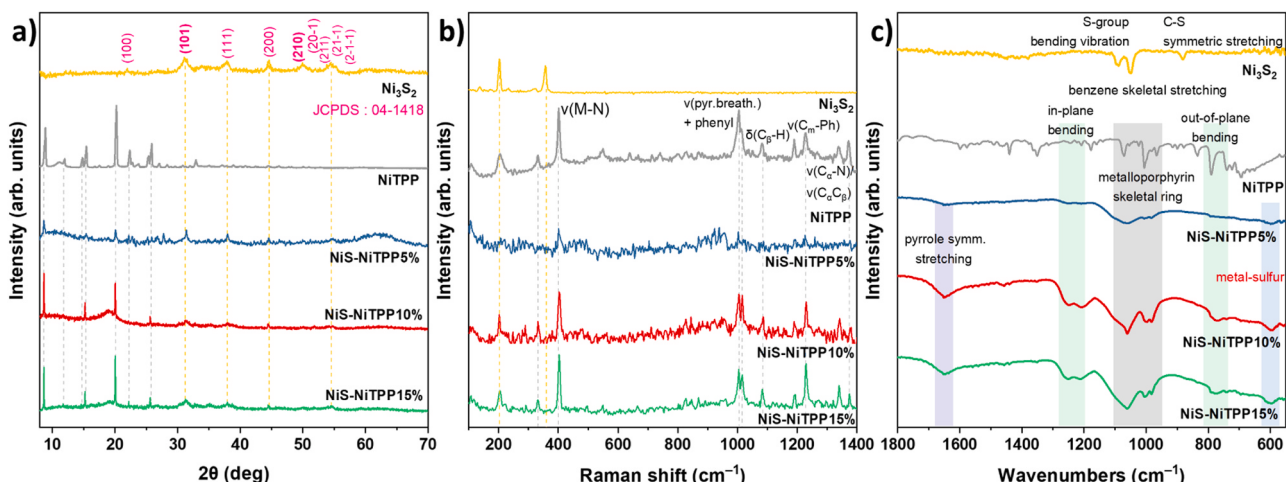


**Fig. 1.** Comprehensive characterization of  $\text{Ni}_3\text{S}_2$ , NiTPP, NiS-NiTPP5%, 10%, and 15% via (a) XRD, (b) Raman, and (c) FTIR analyses.

Apart from these, all materials have characteristic lines of Ni 2p and C 1s. The high-resolution Ni 2p, N 1s, S 2p, and C 1s core-level spectra recorded for Ni<sub>3</sub>S<sub>2</sub>, NiTPP, and NiS-NiTPP10% are depicted in Fig. 2.

In all materials, the Ni 2p level spectra exhibit two distinct peaks at ~856.15 and 873.61 eV with satellites located at 861.84 and 880.06 eV conforming to the 2p<sub>3/2</sub> and 2p<sub>1/2</sub> spin-orbit splitting, respectively (Fig. 2a). The Ni 2p<sub>3/2</sub> peak of the Ni<sub>3</sub>S<sub>2</sub> XPS spectra can be deconvoluted into two peaks detected at 853.3 and 856.1 eV, corresponding to the Ni<sup>2+</sup> and Ni<sup>3+</sup> oxidation states, respectively. However, owing to the metal-like or low-band-gap semiconductor behavior of the crystallographic phase, the 2p<sub>3/2</sub> peak of the Ni<sub>3</sub>S<sub>2</sub> appears closer to the metallic Ni<sup>0</sup> (low BE) [70,71]. In NiTPP, the Ni oxidation state is exclusively 2+, as evident from the peak shift toward higher BE of the Ni 2p<sub>3/2</sub> peak, which is fitted as a single peak at 857 eV, confirming the metalation of TPP with Ni ions. Moreover, the peaks of NiTPP are shifted to higher energy values, owing to the characteristics of the Ni-N bond in the sample. Given the significantly higher electronegativity of N (3.04) compared to Ni (1.91), this disparity induces a shift to higher energies, diverging from the typical signals in the Ni 2p spectrum [72–74]. The presence of Ni<sub>3</sub>S<sub>2</sub> and NiTPP affects the Ni 2p<sub>3/2</sub> component in the Ni 2p spectrum of NiS-NiTPP10%, causing the Ni<sup>2+</sup> and Ni<sup>3+</sup> peaks to shift

slightly from Ni<sub>3</sub>S<sub>2</sub> position to the high binding energy region toward NiTPP (853.5 and 856.4 eV, respectively). A strong signal from nitrogen could be detected only in the NiTPP and NiS-NiTPP10% N 1s spectra shown in Fig. 2b. Considering the structure of NiTPP, where Ni ion is bounded to N, upon deconvolution of Ni 1s, the most pronounced peak observed at 399.5 eV has contributions from Ni-N interaction, followed by iminic N (398.2 eV) and pyrrolic N (402.1 eV). Herein, the N 1s spectrum of NiTPP is typical and in accordance with the structural features of metalloporphyrins obtained in previous studies [74,75]. The presence of sulfur is observed in Ni<sub>3</sub>S<sub>2</sub> and NiS-NiTPP10% as opposed to nitrogen. The S 2p spectra of Ni<sub>3</sub>S<sub>2</sub> and NiS-NiTPP10% shown in Fig. 2c reveal two peaks situated at 163.3 and 168.7 eV, accredited to the sulfide and oxidized sulfate characteristic signals. The peak observed at 163.3 eV can be deconvoluted into two peaks located at 162.9 and 164.3 eV, ascribed to 2p<sub>3/2</sub> and 2p<sub>1/2</sub> orbitals of bridging S<sup>2-</sup> in the Ni-S structure [76,77]. In addition, C 1s spectra were obtained for Ni<sub>3</sub>S<sub>2</sub>, NiTPP, and NiS-NiTPP10% (Fig. 2d). Carbon in Ni<sub>3</sub>S<sub>2</sub> is adventitious, originating from the air exposure of the sample, and the spectrum can be deconvoluted to the C-C (284.8 eV), C-O-C (286.3 eV), and O-C=O (288.8 eV) components. The C 1s spectrum of NiTPP exhibits additional characteristic features at 284.3 (C=C), 286.5 (C-N), and 291.7 eV

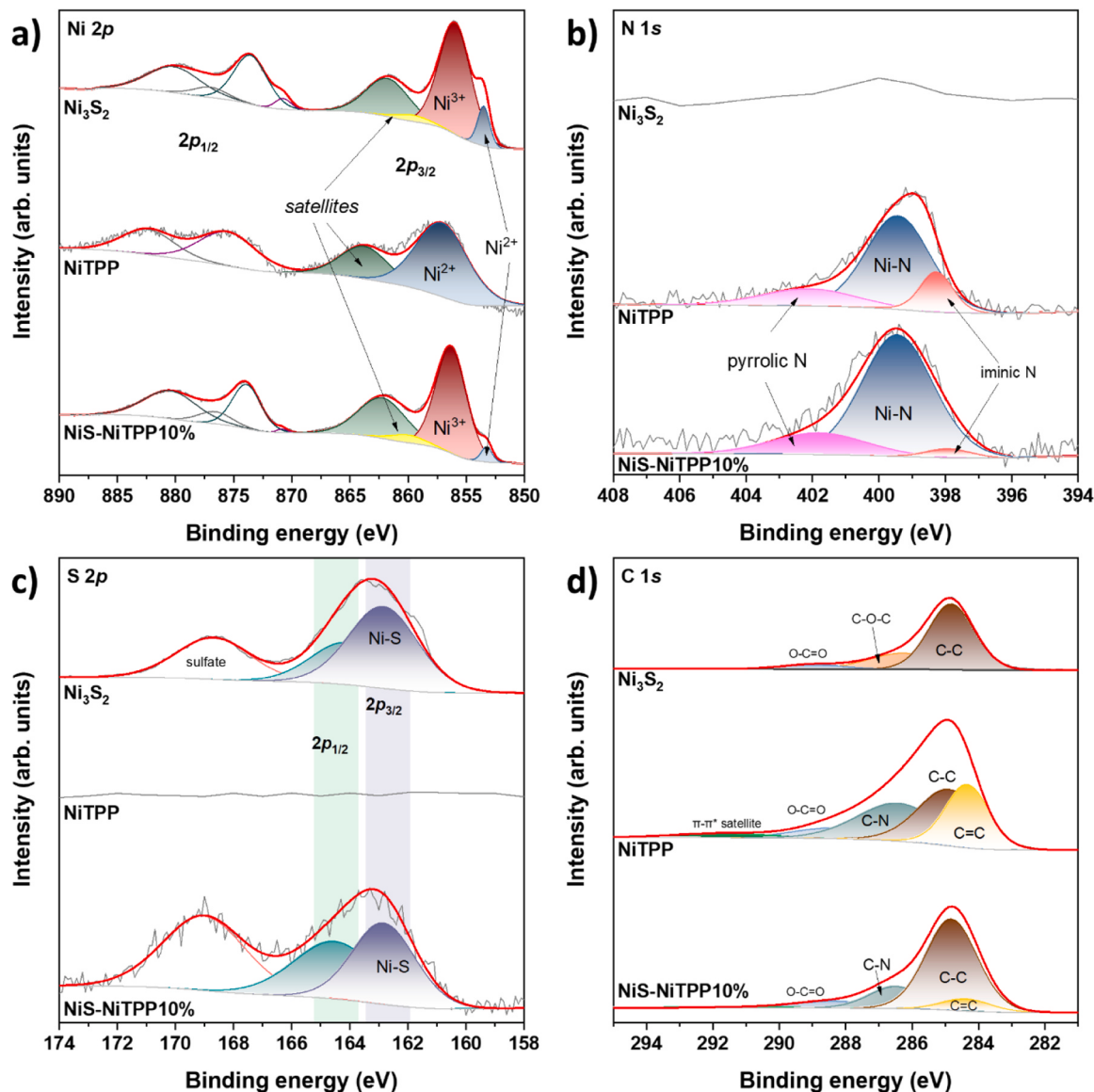
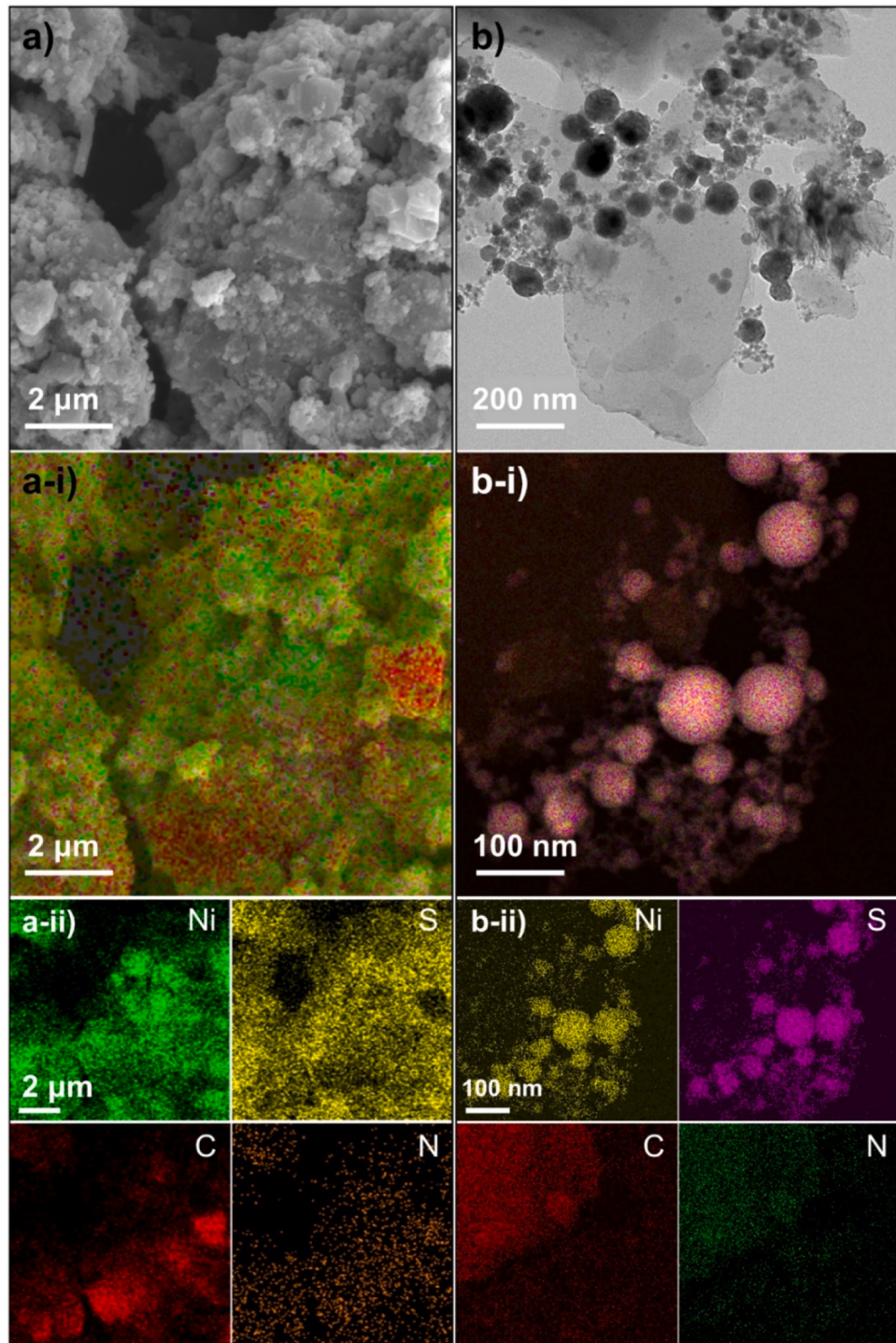


Fig. 2. XPS core-level spectra of (a) Ni 2p, (b) N 1s, (c) S 2p, and (d) C 1s for Ni<sub>3</sub>S<sub>2</sub>, NiTPP, and NiS-NiTPP10% electrocatalysts.

( $\pi-\pi^*$  satellite) owing to the aromatic rings and pyrrole subunits in the structure. The NiS-NiTPP10% composite has the most pronounced and specific features of both  $\text{Ni}_3\text{S}_2$  and NiTPP combined.

Next, the morphology and elemental composition of  $\text{Ni}_3\text{S}_2$ , NiTPP, and NiS-NiTPP10% were examined using field-emission SEM (FE-SEM) equipped with EDS and HRTEM-EDS, and the results are presented in Figs. S3, S4, and 3, respectively. In addition, HAADF-STEM images of bare  $\text{Ni}_3\text{S}_2$  and NiS-NiTPP10% are shown in Figure S5. PLAL-synthesized  $\text{Ni}_3\text{S}_2$  NPs are spherical and comprise homogeneous Ni and S elements throughout the sample, and the morphology and composition were further confirmed via HRTEM analysis (Figure S3). The FE-SEM with

EDS images of NiTPP are shown in Figure S4. NiTPP blocks can be described as bulky, with sizes of tens of microns. EDS analysis detected the presence of Ni, high content of C, and a small amount of N, which agrees with the literature. The HRTEM images of pristine  $\text{Ni}_3\text{S}_2$  and NiTPP are presented in Figure S6. These images elucidate the crystallographic planes, showcasing characteristic  $d$ -spacing values. The measured interplanar distances for  $\text{Ni}_3\text{S}_2$ , corresponding 2.88 Å, 2.37 Å, and 1.83 Å from the (101), (111), and (210) crystallographic planes, respectively, are in well agreement with the XRD data (Figure S6a and Fig. 1a). The NiTPP structure shows the higher  $d$ -spacing value of 4.11 Å originating from the most pronounced peak at 20° in the XRD pattern



**Fig. 3.** The morphological and elemental analysis of the optimized NiS-NiTPP electrocatalyst via (a, a-i, and a-ii) FE-SEM-EDS and (b, b-i, and b-ii) HRTEM-EDS.

(Figure S6b and Fig. 1a). Next, the NiS-NiTPP10% composite was similarly studied using FE-SEM and HRTEM analyses, and images are presented in Fig. 3. Unlike  $\text{Ni}_3\text{S}_2$ , NiS-NiTPP10% contains NiTPP metal-organic blocks, which serve as a substrate for  $\text{Ni}_3\text{S}_2$  NPs evenly spread on it via ultrasonication (Fig. 3a, a-i, and a-ii). Therefore, FE-SEM-EDS and HRTEM-EDS analyses detect the existence of all elements (Ni, S, N, and C) in the final composite (Fig. 3b, b-i, and b-ii). The results of crystallographic, spectroscopic, morphological, and compositional analyses in this study are accurate and consistent with each other and the literature.

### 3.2. Electrochemical $\text{H}_2$ evolution

The ability to drive electrochemical reactions at low potentials with high  $\text{H}_2$  yields was assessed in HER (Fig. 4). LSV curves obtained from three-electrode H-cell compartments in a 0 to  $-0.7$  V vs. RHE in 1.0 M KOH are shown in Fig. 4a. These polarization curves were further used to extract the Tafel graph with estimated Tafel slope values and compare the overpotentials at  $-10$  mA cm $^{-2}$  of the composites (Figs. 4b and 4c, correspondingly). The smallest Tafel slope was obtained for the NiS-NiTPP10% composite (166.6 mV dec $^{-1}$ ), followed by  $\text{Ni}_3\text{S}_2$  (170.4 mV dec $^{-1}$ ), NiS-NiTPP15% (170.6 mV dec $^{-1}$ ), and NiS-NiTPP5% (194.8 mV dec $^{-1}$ ), with the highest slope recorded for NiTPP (272.3 mV dec $^{-1}$ ) (Fig. 4b). Accordingly, the  $\eta$  at  $-10$  mA cm $^{-2}$  gradually increased from the lowest value of 435 (NiS-NiTPP10%), 461 mV (NiS-NiTPP15%), 493 ( $\text{Ni}_3\text{S}_2$ ), and 526 mV (NiS-NiTPP5%) to the highest 596 mV (NiTPP) (Fig. 4c). The Tafel slope value strongly defines the HER kinetics; hence, the rate-decisive step in HER is the hydrogen adsorption step (M-H<sub>ads</sub>) for the electrocatalysts reported in this work ( $\eta > 120$  mV dec $^{-1}$ ) [78]. The NiS-NiTPP10% composite significantly enhances the HER kinetics

compared to the pristine  $\text{Ni}_3\text{S}_2$  and NiTPP. This enhancement is attributed to efficient charge separation and improved synergistic effect between the two materials, resulting in a reduced charge transfer resistance ( $R_{\text{CT}}$ ) at a constant potential of  $-0.3$  V vs. RHE, as demonstrated in the Nyquist plots (Fig. 4d). The  $R_{\text{CT}}$  values, along with the Tafel slope and overpotential values (with the lowest being  $23\ \Omega$  for NiS-NiTPP10%), decrease due to the synergy and strong interaction between  $\text{Ni}_3\text{S}_2$  and NiTPP. This interaction significantly improves HER kinetics. TOF is another parameter that defines the electrocatalytic activity in a particular electrochemical reaction; the higher the TOF, the greater the number of reactant molecules that can be converted into the final product molecules electrochemically. Thus, the active site numbers should be considered from the area under the backward CV curve (Figure S7a-e). Consequently, the NiS-NiTPP10% electrocatalyst, exhibiting the highest Tafel slope and the lowest overpotential, demonstrates the most substantial number of active sites for  $\text{H}_2$  production ( $2.10 \times 10^{16}$ ) at the given potentials of  $-0.4$  V ( $1.17\ \text{s}^{-1}$ ),  $-0.425$  V ( $1.4\ \text{s}^{-1}$ ), and  $-0.45$  V ( $1.7\ \text{s}^{-1}$ ) vs. RHE. This is followed by the NiS-NiTPP15% composite, which shows  $1.92 \times 10^{16}$  active sites, achieving 1.01, 1.25, and  $1.51\ \text{s}^{-1}$  at  $-0.4$ ,  $-0.425$ , and  $0.45$  V vs. RHE (Fig. 4e). The estimated number of active sites for the other three electrocatalysts ( $\text{Ni}_3\text{S}_2$ , NiTPP, and NiS-NiTPP5%) is separately shown in Figure S7f.

In addition to the number of active sites, electrochemically active surface area (ESCA) is another key parameter to assess the performance of electrocatalysts in the electrochemical applications [79]. Therefore, the ESCA values were estimated from the slope of the double-layer capacity ( $C_{\text{dl}}$ ) graph (Figure S8a). The  $C_{\text{dl}}$  slope value was estimated from the CV profiles recorded at scan rates varied from 20 to 100 mV s $^{-1}$  with 20 mV s $^{-1}$  step (Figure S8b-f). To determine the ESCA value of the electrocatalyst, the difference among anodic and cathodic current

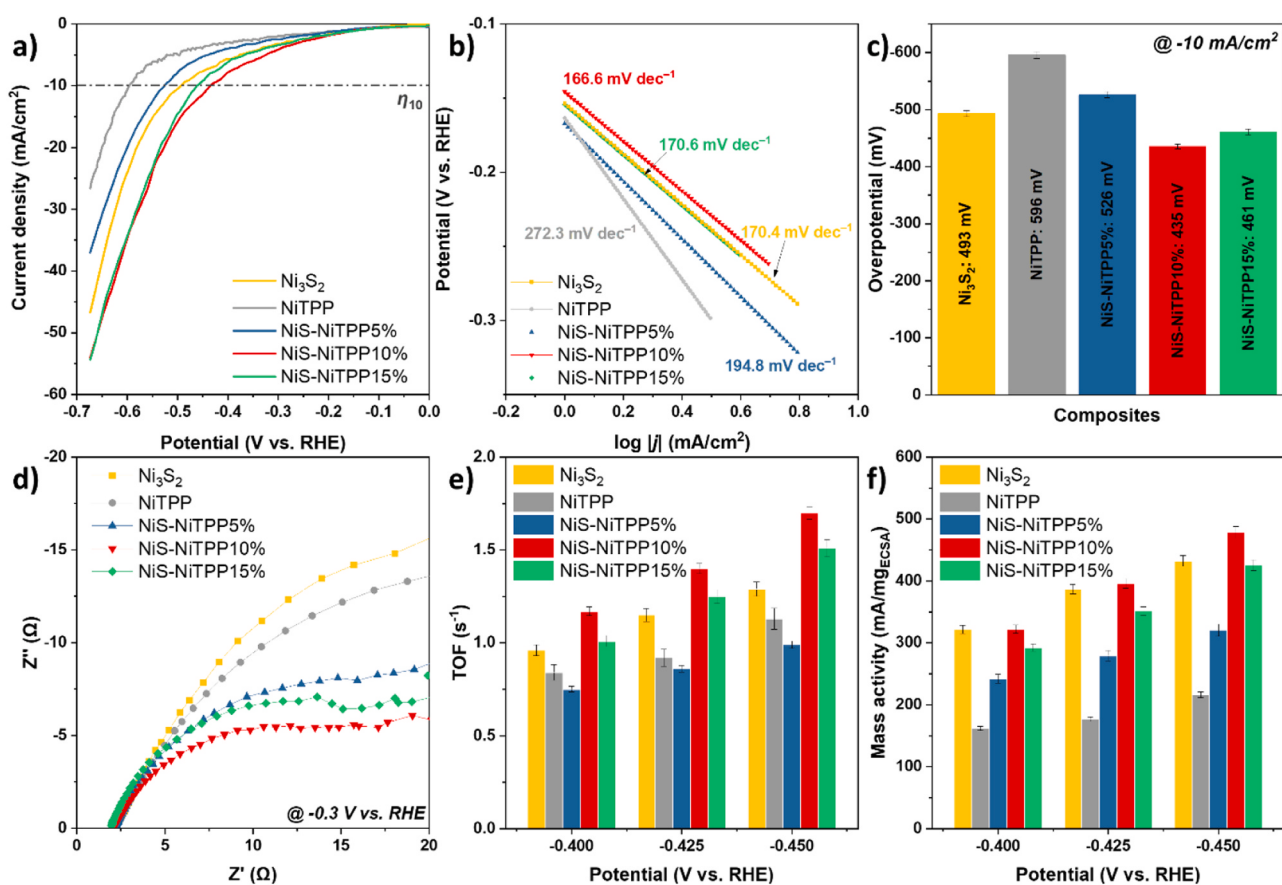


Fig. 4. The HER kinetics of various electrocatalysts in 1 M KOH: (a) LSV, (b) Tafel graphs with considered Tafel slope values, (c)  $\eta$  at  $-10$  mA cm $^{-2}$ , (d) Nyquist plots from electrochemical impedance measured at constant  $-0.3$  V vs. RHE, (e) TOF values, and (f) ECSA-normalized mass activity.

densities versus scan rate is plotted, and half the slope of the linear fitting is calculated. Then, that value is divided by the CC specific capacitance ( $\sim 40 \text{ mF cm}^{-2}$ ) (Figure S8a). As expected, the NiS-NiTPP10% electrocatalyst, characterized by optimized mass loading, enhanced structural properties, and a synergistic effect between two different material groups, exhibits the highest ECSA value of  $26.91 \mu\text{F cm}^{-2}$ , followed by NiS-NiTPP15% ( $19.37 \mu\text{F cm}^{-2}$ ), NiTPP ( $18.38 \mu\text{F cm}^{-2}$ ),  $\text{Ni}_3\text{S}_2$  ( $17.73 \mu\text{F cm}^{-2}$ ), and lastly NiS-NiTPP5% ( $16.52 \mu\text{F cm}^{-2}$ ). The mass activity obtained from the ESCA normalized LSV curves is the final parameter to assess the HER performance of the electrocatalysts (Fig. 4f and S9). By normalizing the LSV curves, we can accurately assess the performance of the composite in the HER. Fig. 4f displays the actual activity of the NiS-NiTPP10%, which demonstrates the highest output current density of  $478.56 \text{ mA mg}_{\text{ECSA}}^{-1}$  at  $-0.45 \text{ V}$  vs. RHE, surpassing the other studied electrocatalysts ( $432.36, 216.38, 320.54$ , and  $425.36 \text{ mA mg}_{\text{ECSA}}^{-1}$  for  $\text{Ni}_3\text{S}_2$ , NiTPP, NiS-NiTPP5%, and NiS-NiTPP15%, respectively). The performance of the NiS-NiTPP10% electrocatalyst is improved owing to the efficient interconnection between HER active  $\text{Ni}_3\text{S}_2$  and NiTPP metal-organic complex with a superior electron transfer capability complements the properties and functions of  $\text{Ni}_3\text{S}_2$ , facilitating the efficient charge transfer for excellent performance [80]. The moderate activity of NiS-NiTPP10% in HER is further evidenced by its comparison with the performance of similar composites reported in the literature, which were synthesized through conventional methods (see Table S1).

### 3.3. Electrochemical OER and AOR

All electrocatalysts in this work were assessed in the oxidation reaction, such as OER, in a three-electrode H-cell compartment at  $1\text{--}1.9 \text{ V}$

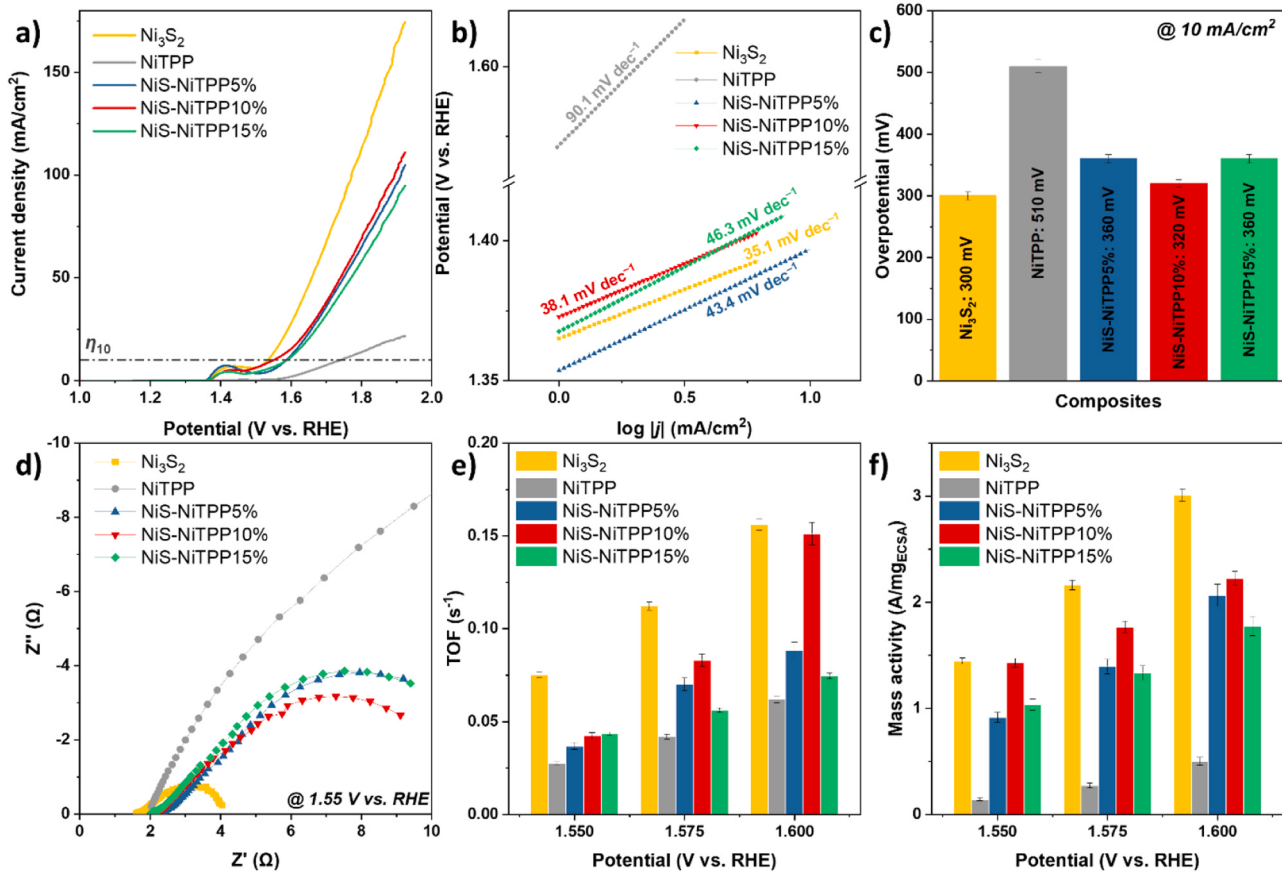


Fig. 5. The OER kinetics of catalysts in 1 M KOH: (a) LSV, (b) derived Tafel graphs with estimated Tafel slope values, (c)  $\eta$  at  $10 \text{ mA cm}^{-2}$ , (d) Nyquist plots from electrochemical impedance measured at a constant  $1.55 \text{ V}$  vs. RHE, (e) TOF values, and (f) ECSA-normalized mass activity.

vs. RHE in  $1.0 \text{ M KOH}$ . First, LSV graphs were attained and exposed in Fig. 5a for each composite. Subsequently, from these curves, Tafel slopes (Fig. 5b) and overpotential values (Fig. 5c) were determined. The  $\text{Ni}_3\text{S}_2$  composite demonstrated the most efficient performance, exhibiting the lowest Tafel slope of  $35.1 \text{ mV dec}^{-1}$  and the lowest  $\eta$  of  $300 \text{ mV}$  at  $10 \text{ mA cm}^{-2}$ . This was closely followed by the NiS-NiTPP10% composite, which was previously identified as the best-performing material in half-cell HER tests, with a Tafel slope value of  $38.1 \text{ mV dec}^{-1}$  and  $\eta$  of  $320 \text{ mV}$ . The NiS-NiTPP5% and NiS-NiTPP15% composites showed comparable performances, each with Tafel slopes of  $43.4$  and  $46.3 \text{ mV dec}^{-1}$ , respectively, and both exhibiting  $\eta \sim 360 \text{ mV}$ . Lastly, the least effective performance was observed in the bare NiTPP, which had a Tafel slope of  $90.1 \text{ mV dec}^{-1}$  and an overpotential of  $510 \text{ mV}$  at  $10 \text{ mA cm}^{-2}$ .

The EIS measurements ( $R_{\text{CT}}$  values) of the electrocatalysts at a constant  $1.55 \text{ V}$  vs. RHE estimates the  $\text{Ni}_3\text{S}_2$  to have the lowest  $R_{\text{CT}}$  value for OER and hence, the fastest charge transfer kinetics, followed by NiS-NiTPP10%, NiS-NiTPP5%, NiS-NiTPP15%, and NiTPP (Fig. 5d). Like the TOF calculation during HER, the OER TOF calculation was performed using the number of active sites extracted from the area under the CV curves recorded in the oxidizing potential range at a constant  $50 \text{ mV s}^{-1}$  sweep rate (Figure S10a–e).  $\text{Ni}_3\text{S}_2$ , displaying the highest number of active sites ( $28.0 \times 10^{16}$  from Figure S10f), consequently exhibits the highest TOF values of  $0.075, 0.112$ , and  $0.156 \text{ s}^{-1}$  at  $1.55, 1.575$ , and  $1.6 \text{ V}$  vs. RHE, respectively (Fig. 5e). NiS-NiTPP10% shows slightly lower TOF values of  $0.042, 0.083$ , and  $0.151 \text{ s}^{-1}$  at the same potentials. In comparison, the TOF values for NiTPP are only  $0.027, 0.041$ , and  $0.062 \text{ s}^{-1}$ , while NiS-NiTPP5% and NiS-NiTPP15% demonstrate TOF values of  $0.037, 0.07$ , and  $0.088 \text{ s}^{-1}$ , and  $0.044, 0.056$ , and  $0.075 \text{ s}^{-1}$  at these potentials, respectively. The ECSA values calculated for these

materials show  $\text{Ni}_3\text{S}_2$  and  $\text{NiS-NiTPP}10\%$  leading with  $9.32$  and  $7.01 \mu\text{F cm}^{-2}$ , respectively, followed by  $\text{NiS-NiTPP}15\%$  at  $6.52 \mu\text{F cm}^{-2}$ ,  $\text{NiS-NiTPP}5\%$  at  $6.01 \mu\text{F cm}^{-2}$ , and  $\text{NiTPP}$  with the lowest value of  $3.99 \mu\text{F cm}^{-2}$  (Figure S11).

The OER performance of the bare electrocatalysts was further assessed through mass activity values obtained from ECSA-normalized LSV curves (Fig. 5f and S12) [81]. Here, a bare  $\text{Ni}_3\text{S}_2$  and  $\text{NiS-NiTPP}10\%$  composite achieved current densities of  $3.01$  and  $2.23 \text{ A mg}_{\text{ECSA}}^{-1}$ , respectively, highlighting their potential for industrial applications. The output current densities for  $\text{NiTPP}$ ,  $\text{NiS-NiTPP}5\%$ , and  $\text{NiS-NiTPP}15\%$  were  $0.5$ ,  $2.07$ , and  $1.78 \text{ A mg}_{\text{ECSA}}^{-1}$ , respectively. Herein, the single-phase  $\text{Ni}_3\text{S}_2$  exhibits better OER activity than the composites with certain  $\text{NiTPP}$  ratios (i.e.,  $5 \text{ wt\%}$ ,  $10 \text{ wt\%}$ , and  $15 \text{ wt\%}$ ). Hence, there is some inhibiting effect from the  $\text{NiTPP}$  metal-organic complex that regards the performance of a composite. Metalloporphyrins are excellent electrocatalysts for the ORR. This could be owing to the affinity of  $\text{NiTPP}$  to bind  $\text{O}_2$  molecules, which prevent the active sites from oxidizing water and releasing  $\text{O}_2$  as gas. Instead, the  $\text{O}_2$  molecules are bound to the surface of the electrocatalyst. Despite the poor OER performance, metalloporphyrins can be highly selective toward the electrooxidation reactions of organic substance, such as  $\text{B.Alc}$  electrooxidation at low potentials [73,82–84]. Moreover,  $\text{Ni}_3\text{S}_2$  materials were also used as electrocatalysts in the alcohol electrochemical oxidation reaction [85–87]. Considering this,  $\text{NiS-NiTPP}$  composites were used as electrocatalysts for the AOR to selectively produce targeted  $\text{B.Ac}$  from  $\text{B.Alc}$  (Fig. 6). LSV curves were recorded in a three-electrode H-cell compartment with  $1.0 \text{ M KOH}$  and  $1.0 \text{ M KOH}$  with  $10 \text{ mM B.Alc}$  were used as anolyte in the potential range of  $1$ – $1.9 \text{ V}$  vs. RHE (Fig. 6a, S13, and S14a). Polarization curves shift toward the low potential, and

high current densities can be achieved when  $10 \text{ mM B.Alc}$  is in the anolyte, confirming the oxidation of  $\text{B.Alc}$  to be more energetically beneficial than the OER process (Figures S13 and S14). This also leads to a decrease in overpotential value, where adding only  $10 \text{ mM B.Alc}$  into the anolyte decreases the overpotentials of AOR over  $\text{Ni}_3\text{S}_2$ ,  $\text{NiTPP}$ ,  $\text{NiS-NiTPP}5\%$ ,  $\text{NiS-NiTPP}10\%$ , and  $\text{NiS-NiTPP}15\%$  from  $300$  to  $170 \text{ mV}$ ,  $510$ – $515 \text{ mV}$ ,  $360$ – $165 \text{ mV}$ ,  $320$ – $170 \text{ mV}$ , and  $360$ – $200 \text{ mV}$ , respectively (Figure S14b). Among the composites in this work,  $\text{NiS-NiTPP}10\%$  shows the highest current density of  $24.43 \text{ mA cm}^{-2}$  at a given  $1.53 \text{ V}$  vs. RHE in AOR compared with  $17.9$  ( $\text{Ni}_3\text{S}_2$ ),  $4.04$  ( $\text{NiTPP}$ ),  $18.31$  ( $\text{NiS-NiTPP}5\%$ ), and  $12.78 \text{ mA cm}^{-2}$  ( $\text{NiS-NiTPP}15\%$ ) (Fig. 6b). Hence, considering the  $\text{NiS-NiTPP}10\%$  as the best-performing electrocatalyst, the AOR was assessed at different potentials of  $1.4$ ,  $1.45$ , and  $1.5 \text{ V}$  vs. RHE to determine at which potential  $\text{NiS-NiTPP}10\%$  composite shows its best performance and comparison over other composites were examined (Figure S15).

The HPLC analysis after AOR at different potentials shown in Figure S15a and Figure S16 demonstrated that the  $\text{B.Ac}$  production reached the saturation at some potential ( $>1.45 \text{ V}$  vs. RHE), producing the byproduct, such as  $\text{B.Ald}$  at  $1.5 \text{ V}$  vs. RHE. The HPLC analysis of the standard of  $\text{B.Alc}$ ,  $\text{B.Ac}$ , and  $\text{B.Ald}$  solutions with known concentrations of  $1$ ,  $2$ ,  $5$ , and  $10 \text{ mM}$  were performed before AOR experiments, and the corresponding calibration curves were obtained (Figure S17). The analysis of AOR kinetics revealed that  $24.6\%$  of  $\text{B.Alc}$  was electrochemically converted to the  $\text{B.Ac}$  and the intermediate  $\text{B.Ald}$  with the highest reaction rate ( $k_{\text{app}}$ ) of  $4.35 \mu\text{M min}^{-1}$  at  $1.45 \text{ V}$  vs. RHE ( $18.9\%$  of  $\text{B.Alc}$  conversion with  $k_{\text{app}} = 3.14 \mu\text{M min}^{-1}$  and  $25.1\%$  conversion with  $k_{\text{app}} = 4.32 \mu\text{M min}^{-1}$  at  $1.4$  and  $1.5 \text{ V}$  vs. RHE, correspondingly) (Figure S15b–d). The reaction parameters, such as mass balance, FE, and

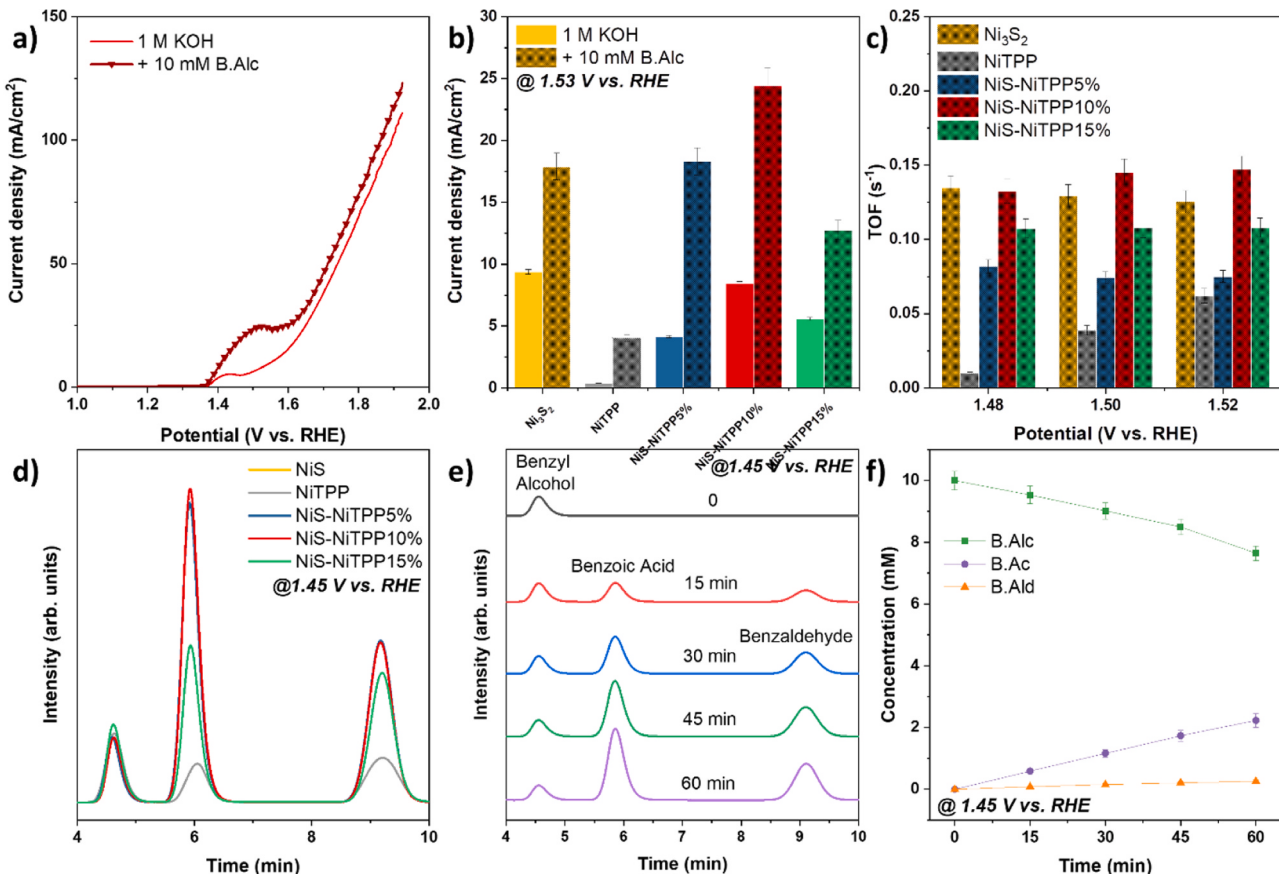


Fig. 6. AOR at optimal  $1.45 \text{ V}$  vs. RHE. (a) The LSV curves of  $\text{NiS-NiTPP}10\%$  recorded in  $1.0 \text{ M KOH}$  and in  $1.0 \text{ M KOH}$  with  $10 \text{ mM}$  of  $\text{B.Alc}$ , (b) a comparison of output current density at a selected  $1.53 \text{ V}$  vs. RHE potential, (c) the TOF values for AOR in  $10 \text{ mM B.Alc}$  at selected  $1.48$ ,  $1.50$ , and  $1.52 \text{ V}$  vs. RHE, (d) the HPLC profiles after  $1 \text{ h}$  of AOR with different electrocatalysts at constant  $1.45 \text{ V}$  vs. RHE, (e) the time-resolved HPLC profiles of AOR over the best-performing  $\text{NiS-NiTPP}10\%$  at  $1.45 \text{ V}$  vs. RHE and, (f) time-resolved conversion of  $\text{B.Alc}$  to  $\text{B.Ac}$  via the intermediate  $\text{B.Ald}$ .

selectivity, define the electrocatalyst; thus, 1.45 V vs. RHE was selected as the optimal potential for AOR tests in this study, at which NiS-NiTPP10% exhibited the best performance with 100% mass balance, 98.3% FE, and 99.8% selectivity toward value-added B.Ac production (vs. 100%, 99.9%, and 99.3% at 1.4 V vs. RHE and 100%, 91.8%, and 94.9% at 1.5 V vs. RHE, respectively) (Figures S15e and S15f).

To assess the ability of a single active site in the composite to oxidize molecules of B.Alc to B.Ac with high efficiency, TOF values were calculated using the number of active sites at 1.48, 1.50, and 1.52 V vs. RHE (Fig. 6c and S18). As expected, NiS-NiTPP10% reached the highest TOF values of 0.132, 0.145, and 0.147  $s^{-1}$  at 1.48, 1.50, and 1.52 V vs. RHE, respectively, followed by Ni<sub>3</sub>S<sub>2</sub> with 0.132, 0.129, and 0.125  $s^{-1}$ , NiS-NiTPP15% with 0.107, 0.108, and 0.108  $s^{-1}$ , NiS-NiTPP5% with 0.082, 0.074, and 0.075  $s^{-1}$ , and finally NiTPP with 0.01, 0.039, and 0.062  $s^{-1}$ , respectively. The superior performance of NiS-NiTPP10% can also be observed from the HPLC profiles, where the B.Ac peak area is higher than the other composites in this work (Figs. 6d, 7e, and S19). The time-resolved conversion of B.Alc to targeted B.Ac over NiS-NiTPP10% shown in Fig. 6f indicates that the B.Ald is not yielding as a final product but as an intermediate state in the alcohol to the acid conversion reaction. The reaction kinetics and key parameters were calculated for the electrocatalysts used in this work and presented in Fig. 7. NiS-NiTPP10% showed the highest B.Alc conversion rate of 4.35  $\mu\text{M min}^{-1}$  (23.56% of B.Alc converted to B.Ac), followed by Ni<sub>3</sub>S<sub>2</sub> with 4.18  $\mu\text{M min}^{-1}$  (22.24%), NiS-NiTPP5% with 4.1  $\mu\text{M min}^{-1}$  (22.84%), NiS-NiTPP15% with 2.56  $\mu\text{M min}^{-1}$  (14.1%), and NiTPP with 0.59  $\mu\text{M min}^{-1}$  (3.33%) at 1.45 V vs. RHE (Figs. 7a and 7b). The yields of B.Ac and B.Ald from AOR were calculated and given in Fig. 7c, where the highest 2.23 mM (0.26 B.Ald) of B.Ac was produced during AOR with NiS-NiTPP10% composite, followed by Ni<sub>3</sub>S<sub>2</sub>, NiS-NiTPP5%, NiS-NiTPP15%, NiTPP electrocatalyst with 1.87 (0.23), 1.21 (0.12), 1.12

(0.21), and 0.35 mM (0.1 mM), respectively. Overall, the B.Ac yield rate can reach up to 2.23 mM  $\text{h}^{-1} \text{cm}^{-2}$  accordingly (Fig. 7d). Finally, mass balance, FE, and selectivity toward B.Ac and B.Ald were estimated and displayed in Figs. 7e and 7f.

The mass balance of AOR is ~100% for all the composites, indicating a simple, straightforward B.Alc oxidation to B.Ac compared to OER or other complex organic system oxidation. The calculated FE values were 95.3%, 91.2%, 98.9%, 98.3, and 85.2% for Ni<sub>3</sub>S<sub>2</sub>, NiTPP, NiS-NiTPP5%, NiS-NiTPP10%, and NiS-NiTPP15%, respectively, which can be considered as excellent performance. However, the most important parameter of an electrocatalyst is its selectivity toward the targeted and value-added product of the reaction, such as B.Ac. Therefore, the NiS-NiTPP10% composite was highlighted as the best electrocatalyst for the highly selective (99.8%) and efficient (98.3%) B.Ac production from the electrocatalytic oxidation of B.Alc. Other composites exhibited low selectivity of 79.6%, 96.3%, 93.5%, and 83.8% for Ni<sub>3</sub>S<sub>2</sub>, NiTPP, NiS-NiTPP5%, and NiS-NiTPP15%, respectively. The selectivity of electrocatalysts toward the intermediate B.Ald remains nearly the same and stays as low as 10%–15%. The OER and AOR performance of NiS-NiTPP10% was evaluated and found to be consistent with the performance of previously reported composites, as detailed in Table S1 and Table S2, respectively. The overall comparative performance of electrocatalysts in HER, OER, and AOR is organized in Figure S20. All composites reported in this study can drive electrochemical HER, OER, and AOR efficiently except for the bare NiTPP metal–organic complex owing to its origin, in most cases acting as a substrate and an additive to the main electrocatalysts to enhance the charge transfer kinetics and the most important selectivity. Therefore, the composite with 5 wt%, 10 wt %, and 15 wt% of NiTPP and Ni<sub>3</sub>S<sub>2</sub> shows enhanced selectivity toward a single product of AOR.

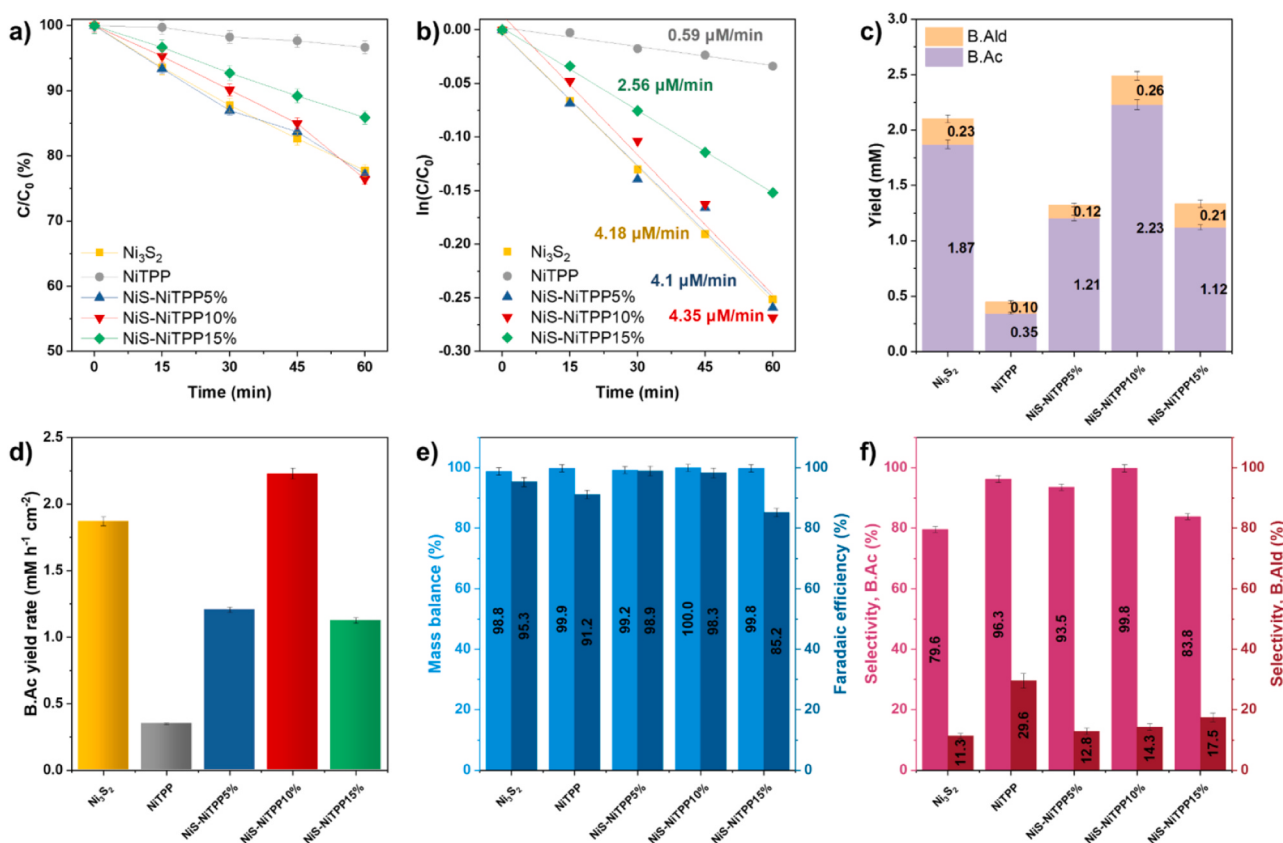


**Fig. 7.** AOR kinetics and parameters. (a) The conversion of B.Alc, (b) reaction kinetics with calculated  $k_{\text{app}}$  values, (c) B.Ac and B.Ald yields, (d) B.Ac yield rate, (e) mass balance and FE, and (f) selectivity toward B.Ac and intermediate B.Ald for the AOR with Ni<sub>3</sub>S<sub>2</sub>, NiTPP, NiS-NiTPP5%, NiS-NiTPP10%, and NiS-NiTPP15% at constant 1.45 V vs. RHE.

### 3.4. Symmetric tandem hybrid electrolyzer (HER|| AOR)

Finally, the symmetric hybrid electrolyzer was set up for simultaneous H<sub>2</sub> gas evolution during HER in the cathode compartment and value-added B.Ac production during AOR in the anode compartment. Electrocatalysts were used as both cathode and anode, and LSV curves were recorded at the cell voltage from 0 to 2.7 V (Fig. 8a and S21). Replacing the sluggish OER with AOR in the anode compartment visibly improves the electrolyzer efficiency by lowering the cell voltage to 193 mV in the NiS-NiTPP10%||NiS-NiTPP10% hybrid electrolyzer (Fig. 8b). It further leads to the energy-saving production of H<sub>2</sub> gas with a yield rate of 0.42 mM h<sup>-1</sup> cm<sup>-2</sup> and a large FE of 81% simultaneously with the production of B.Ac at 4.03 mM h<sup>-1</sup> cm<sup>-2</sup> rate with a FE of 99% during continuous 2 h bulk electrolysis at a constant cell voltage (Fig. 8c, S22, and S23). High-purity H<sub>2</sub> gas of known volume (50, 100, 150, 200, and 250  $\mu$ L) was measured via GC to obtain the calibration curve before the experiments (Figure S24).

Combining Ni<sub>3</sub>S<sub>2</sub> and NiTPP can result in a synergistic effect that enhances the electrocatalytic activity of AOR. The proposed mechanism for the NiS-NiTPP10% composite effectively driving the AOR reaction is presented in Fig. 8d, where the four elementary stages (Fig. 8d (i)–(iv)) are highlighted. The high surface area of Ni<sub>3</sub>S<sub>2</sub>, characterized by an increased number of active sites under oxidizing conditions as established in the OER study, in conjunction with the superior electron transfer properties of NiTPP in the NiS-NiTPP10% composite, is believed to foster this synergy. This combination facilitates the capture and selective oxidation of B.Ac, as illustrated in Fig. 8d, stage (i). The presence of electron-rich pyrrole rings in the porphyrin macrocycle of NiTPP is believed to activate B.Alc by coordinating with its alcohol group. This coordination assists in forming the B.Ald intermediate via the reaction B.Alc  $\rightarrow$  B.Ald + H<sup>+</sup> + e<sup>-</sup>. The electrons released during this process are transferred through the external circuit to the cathodic compartment, as depicted in Fig. 8d, stage (ii). It is then postulated that the B.Ald intermediate coordinates with the Ni centers on the NiS-NiTPP10% surface through its carbonyl oxygen atom, as shown in Fig. 8d, stage (iii). The subsequent oxidation of B.Ald at the Ni redox pairs on the anode surface to produce B.Ac, through the reaction B.Ald + H<sub>2</sub>O  $\rightarrow$  B.Ac + H<sup>+</sup> + 2e<sup>-</sup>, is detailed in Fig. 8d, stage (iv). This reaction incorporates a water molecule and consumes two electrons [82,88–90]. The active role of Ni<sup>2+</sup>/Ni<sup>3+</sup> centers in the AOR process is evidenced by the post-AOR Ni 2p high-resolution XPS spectrum of the NiS-NiTPP10% composite. A

shift in the intensity ratio of Ni<sup>2+</sup> and Ni<sup>3+</sup> peaks, with a predominance of Ni<sup>2+</sup> centers post-reaction, suggests the reduction of Ni<sup>3+</sup> to Ni<sup>2+</sup>, a change consistent with the transient formation of NiOOH and Ni(OH)<sub>2</sub> surface reactive phases and the corresponding oxidation of B.Alc to B.Ac during the redox process [91,92]. It was assumed that the suggested mechanism could be acceptable at specific reaction conditions and experimental parameters in this study. The stability of the NiS-NiTPP10% electrocatalyst after AOR was assessed by comparing the XPS core-level spectra of Ni 2p, N 1s, S 2p, and C 1s before and after AOR analysis (Figure S25). This analysis reveals the partial oxidation of Ni centers in the NiS-NiTPP10% composite to NiOOH and Ni(OH)<sub>2</sub> species, which are implicated in the oxidation of B.Alc in 1.0 M KOH alkaline medium. This process significantly contributes to the observed shifts in the Ni<sup>2+</sup>/Ni<sup>3+</sup> ratios in Ni 2p and sulfate peak in the S 2p spectrum of the composite after the AOR. The comparison of NiS-NiTPP10% composite with reported materials toward electrochemical oxidation of B.Alc is given in Table S2, and the FE, selectivity, and yield rate values obtained in this work are similar and even superior to some of the reported values.

### 4. Conclusion

PLAL-synthesized single-phase Ni<sub>3</sub>S<sub>2</sub> was successfully combined with 5 wt%, 10 wt%, and 15 wt% of NiTPP metal–organic complex to obtain a highly selective and efficient electrocatalyst. The metalation of TPP and further interaction with Ni<sub>3</sub>S<sub>2</sub> was thoroughly studied via structural and compositional characterization. The performance of the composites was assessed in consecutive HER, OER, and AOR, in which NiS-NiTPP10% exhibited the highest activity achieving 435, 320, and 170 mV overpotentials, respectively. Moreover, NiS-NiTPP10% was found to favor AOR and produce B.Ac at 2.23 mM h<sup>-1</sup> cm<sup>-2</sup> yield rate with 100% mass balance, 98.3% FE, and 99.8% selectivity. Finally, the system with simultaneous H<sub>2</sub> evolution and value-added B.Ac production was successfully constructed over the NiS-NiTPP10%||NiS-NiTPP10% and achieved a high FE of 81% and 99% and yield rates of 0.42 and 4.03 mM h<sup>-1</sup> cm<sup>-2</sup>, respectively.

### CRedit authorship contribution statement

**Ahreum Min:** Writing – review & editing, Validation, Formal analysis. **Jayaraman Theerthagiri:** Writing – original draft, Validation, Investigation, Conceptualization. **Talshyn Begildayeva:** Writing –

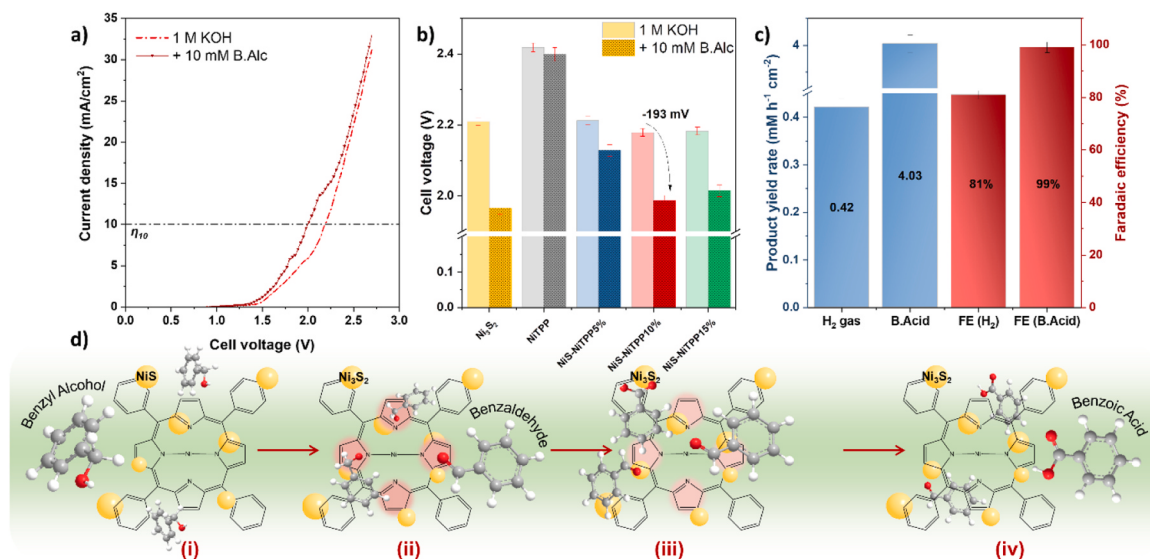


**Fig. 8.** The symmetric hybrid electrolyzer (HER||AOR). (a) LSV curves recorded in electrolyzer with NiS-NiTPP10%||NiS-NiTPP10% couple in 1.0 M KOH and 1.0 M KOH with 10 mM B.Alc, (b) corresponding cell voltages, (c) H<sub>2</sub> and B.Ac product yields and FE, and (d) proposed mechanism for AOR with the best-performing NiS-NiTPP10% electrocatalyst.

original draft, Methodology, Investigation, Data curation, Conceptualization. **Myong Yong Choi**: Writing – review & editing, Supervision, Resources, Project administration, Funding acquisition. **Cheol Joo Moon**: Writing – review & editing, Visualization, Investigation.

## Declaration of Competing Interest

The authors declare that they have no known competing financial interests or personal relationships that could have appeared to influence the work reported in this paper.

## Data availability

Data will be made available on request.

## Acknowledgements

This research was supported by Korea Basic Science Institute (National research Facilities and Equipment Center) grant funded by the Ministry of Education. (No. 2019R1A6C1010042, 2021R1A6C103A427). The authors acknowledge the financial support from National Research Foundation of Korea (NRF), (2022R1A2C2010686, 2022R1A4A3033528, 2021R1I1A1A01060380, 2019H1D3A1A01071209, 2021R1C1C2010726).

## Appendix A. Supporting information

Supplementary data associated with this article can be found in the online version at [doi:10.1016/j.apcatb.2024.123907](https://doi.org/10.1016/j.apcatb.2024.123907).

## References

- [1] C. Duan, C. Tang, S. Yu, L. Li, J. Li, Y. Zhou, Efficient electrocatalytic desulfurization and synchronous hydrogen evolution from  $H_2S$  via anti-sulfuretted NiSe nanowire array catalyst, *Appl. Catal. B: Environ.* 324 (2023) 122255.
- [2] Q. Yu, Y. Fu, J. Zhao, B. Li, X. Wang, X. Liu, L. Wang, Boron doping activate strong metal-support interaction for electrocatalytic hydrogen evolution reaction in full pH range, *Appl. Catal. B: Environ.* 324 (2023) 122297.
- [3] W. Wang, L. Kuai, W. Cao, M. Huttula, S. Ollikkala, T. Ahopelto, A.-P. Honkanen, S. Huotari, M. Yu, B. Geng, Mass-Production of Mesoporous  $MnCo_2O_4$  Spines with Manganese(IV)- and Cobalt(II)-Rich Surfaces for Superior Bifunctional Oxygen Electrocatalysis, *Angew. Chem. Int. Ed.* 56 (2017) 14977–14981.
- [4] L. Wang, J. Geng, W. Wang, C. Yuan, L. Kuai, B. Geng, Facile synthesis of Fe/Ni bimetallic oxide solid-solution nanoparticle with superior electrocatalytic activity for oxygen evolution reaction, *Nano Res.* 8 (2015) 3815–3822.
- [5] Y. Gao, S. Qian, H. Wang, W. Yuan, Y. Fan, N. Cheng, H. Xue, T. Jiang, J. Tian, Boron-doping on the surface mediated low-valence Co centers in cobalt phosphide for improved electrocatalytic hydrogen evolution, *Appl. Catal. B: Environ.* 320 (2023) 122014.
- [6] M.-Y. Qi, M. Conte, M. Anpo, Z.-R. Tang, Y.-J. Xu, Cooperative Coupling of Oxidative Organic Synthesis and Hydrogen Production over Semiconductor-Based Photocatalysts, *Chem. Rev.* 121 (2021) 13051–13085.
- [7] N.-T. Suen, S.-F. Hung, Q. Quan, N. Zhang, Y.-J. Xu, H.M. Chen, Electrocatalysis for the oxygen evolution reaction: recent development and future perspectives, *Chem. Soc. Rev.* 46 (2017) 337–365.
- [8] C. Xiao, L. Zhang, H. Hao, W. Wang, High Selective Oxidation of Benzyl Alcohol to Benzylaldehyde and Benzoic Acid with Surface Oxygen Vacancies on  $W_{18}O_{49}/$  Holey Ultrathin  $g\text{-}C_3N_4$  Nanosheets, *ACS Sustain. Chem. Eng.* 7 (2019) 7268–7276.
- [9] M.C.M. Libanori, G.G. Santos, S.A. Pereira, J.V.S. Ferrarezi, M.B. Ferreira, L. Cardoso, D.S. Costa, M. Fernandes, K.A. Gomes, M. Tedesco, T.A. Soligo, E. Yamashita, M.L. Martins, J.L.P. Mourão, Organic benzoic acid modulates health and gut microbiota of *Oreochromis niloticus*, *Aquaculture* 570 (2023) 739409.
- [10] X. Yang, R. Sun, Progress in Transition-Metal-Catalyzed Synthesis of Benzo-Fused Oxygen- and Nitrogen Heterocyclic Compounds from Benzoic Acids, *Adv. Synth. Catal.* 365 (2023) 124–141.
- [11] L. Zhu, Y. Luo, Y. He, M. Yang, Y. Zhang, M. Fan, Q. Li, Selective catalytic synthesis of bio-based high value chemical of benzoic acid from xylan with  $Co_2MnO_4@MCM-41$  catalyst, *Molecular, Catalysis* 517 (2022) 112063.
- [12] X. Zhang, W. Huang, L. Yu, M. García-Melchor, D. Wang, L. Zhi, H. Zhang, Enabling heterogeneous catalysis to achieve carbon neutrality: Directional catalytic conversion of  $CO_2$  into carboxylic acids, *Carbon Energy* (n/a) (2023) e362.
- [13] Z. Li, Y. Yan, S.-M. Xu, H. Zhou, M. Xu, L. Ma, M. Shao, X. Kong, B. Wang, L. Zheng, H. Duan, Alcohols electrooxidation coupled with  $H_2$  production at high current densities promoted by a cooperative catalyst, *Nature, Communications* 13 (2022) 147.
- [14] G. Liu, X. Zhang, C. Zhao, Q. Xiong, W. Gong, G. Wang, Y. Zhang, H. Zhang, H. Zhao, Electrocatalytic oxidation of benzyl alcohol for simultaneously promoting  $H_2$  evolution by a  $Co_{0.83}Ni_{0.17}/$ activated carbon electrocatalyst, *N. J. Chem.* 42 (2018) 6381–6388.
- [15] N. Shilpa, A. Pandikassala, P. Krishnaraj, P.S. Walko, R.N. Devi, S. Kurungot, Co-Ni Layered Double Hydroxide for the Electrocatalytic Oxidation of Organic Molecules: An Approach to Lowering the Overall Cell Voltage for the Water Splitting Process, *ACS Appl. Mater. Interfaces* 14 (2022) 16222–16232.
- [16] C. Zheng, G. He, X. Xiao, M. Lu, H. Zhong, X. Zuo, J. Nan, Selective photocatalytic oxidation of benzyl alcohol into benzaldehyde with high selectivity and conversion ratio over  $Bi_4O_3Br_2$  nanoflakes under blue LED irradiation, *Appl. Catal. B: Environ.* 205 (2017) 201–210.
- [17] E.K. Joice, S. Rison, K.B. Akshaya, A. Varghese, Platinum decorated polythiophene modified stainless steel for electrocatalytic oxidation of benzyl alcohol, *J. Appl. Electrochem.* 49 (2019) 937–947.
- [18] G. Zhao, F. Yang, Z. Chen, Q. Liu, Y. Ji, Y. Zhang, Z. Niu, J. Mao, X. Bao, P. Hu, Y. Li, Metal/oxide interfacial effects on the selective oxidation of primary alcohols, *Nature, Communications* 8 (2017) 14039.
- [19] Z. Wang, J. Shi, D. Wang, Y. Pu, J.-X. Wang, J.-F. Chen, Metal-free catalytic oxidation of benzylic alcohols for benzaldehyde, *React. Chem. Eng.* 4 (2019) 507–515.
- [20] C.S. Ramirez-Barria, M. Isaacs, C. Parlett, K. Wilson, A. Guerrero-Ruiz, I. Rodriguez-Ramos, Ru nanoparticles supported on N-doped reduced graphene oxide as valuable catalyst for the selective aerobic oxidation of benzyl alcohol, *Catal. Today* 357 (2020) 8–14.
- [21] H. He, A. Liao, W. Guo, W. Luo, Y. Zhou, Z. Zou, State-of-the-art progress in the use of ternary metal oxides as photoelectrode materials for water splitting and organic synthesis, *Nano Today* 28 (2019) 100763.
- [22] Y. Wang, B. Kong, D. Zhao, H. Wang, C. Selomulya, Strategies for developing transition metal phosphides as heterogeneous electrocatalysts for water splitting, *Nano Today* 15 (2017) 26–55.
- [23] Y. Chen, Y. Yang, X. Liu, X. Shi, C. Wang, H. Zhong, F. Jin, Sustainable production of formic acid and acetic acid from biomass, *Mol. Catal.* 545 (2023) 113199.
- [24] F.-K. Shang, Y.-H. Li, M.-Y. Qi, Z.-R. Tang, Y.-J. Xu, Photocatalytic materials for sustainable chemistry via cooperative photoredox catalysis, *Catal. Today* 410 (2023) 85–101.
- [25] M.-H. Sun, M.-Y. Qi, C.-L. Tan, Z.-R. Tang, Y.-J. Xu, Interfacial engineering of  $CdS$  for efficient coupling photoredox, *Chin. Chem. Lett.* 34 (2023) 108022.
- [26] Q. Hua, K.E. Madsen, A.M. Esposito, X. Chen, T.J. Woods, R.T. Haasch, S. Xiang, A. I. Frenkel, T.T. Fister, A.A. Gewirth, Effect of Support on Oxygen Reduction Reaction Activity of Supported Iron Porphyrins, *ACS, Catalysis* 12 (2022) 1139–1149.
- [27] A. Singha, A. Mondal, A. Nayek, S.G. Dey, A. Dey, Oxygen Reduction by Iron Porphyrins with Covalently Attached Pendent Phenol and Quinol, *J. Am. Chem. Soc.* 142 (2020) 21810–21828.
- [28] P. Chou, L. Kim, S.M. Marzouk, R. Sun, A.C. Hartnett, D.K. Dogutan, S.-L. Zheng, D. G. Nocera, Synthesis, Characterization, and Hydrogen Evolution Activity of Metallo-meso-(4-fluoro-2,6-dimethylphenyl)porphyrin Derivatives, *ACS Omega* 7 (2022) 8988–8994.
- [29] Z. Liang, H. Guo, H. Lei, R. Cao, Co porphyrin-based metal-organic framework for hydrogen evolution reaction and oxygen reduction reaction, *Chin. Chem. Lett.* 33 (2022) 3999–4002.
- [30] X. Li, H. Lei, L. Xie, N. Wang, W. Zhang, R. Cao, Metalloporphyrins as Catalytic Models for Studying Hydrogen and Oxygen Evolution and Oxygen Reduction Reactions, *Acc. Chem. Res.* 55 (2022) 878–892.
- [31] Z. Liang, H.-Y. Wang, H. Zheng, W. Zhang, R. Cao, Porphyrin-based frameworks for oxygen electrocatalysis and catalytic reduction of carbon dioxide, *Chem. Soc. Rev.* 50 (2021) 2540–2581.
- [32] W. Zhang, W. Lai, R. Cao, Energy-Related Small Molecule Activation Reactions: Oxygen Reduction and Hydrogen and Oxygen Evolution Reactions Catalyzed by Porphyrin- and Corrole-Based Systems, *Chem. Rev.* 117 (2017) 3717–3797.
- [33] W. Moschkowitsch, B. Samanta, N. Zion, H.C. Honig, D.A. Cullen, M. Caspary-Toroker, L. Elbaz, NiFe-mixed metal porphyrin aerogels as oxygen evolution reaction catalysts in alkaline electrolyzers, *Nanoscale* 14 (2022) 18033–18040.
- [34] Q. Lin, X. Bu, A. Kong, C. Mao, F. Bu, P. Feng, Heterometal-Embedded Organic Conjugate Frameworks from Alternating Monomeric Iron and Cobalt Metalloporphyrins and Their Application in Design of Porous Carbon Catalysts, *Adv. Mater.* 27 (2015) 3431–3436.
- [35] D.K. Perivoliotis, J. Ekspong, X. Zhao, G. Hu, T. Wågberg, E. Gracia-Espino, Recent progress on defect-rich electrocatalysts for hydrogen and oxygen evolution reactions, *Nano Today* 50 (2023) 101883.
- [36] D.Y. Chung, J.W. Han, D.-H. Lim, J.-H. Jo, S.J. Yoo, H. Lee, Y.-E. Sung, Structure dependent active sites of  $Ni_3S_2$  as electrocatalysts for hydrogen evolution reaction, *Nanoscale* 7 (2015) 5157–5163.
- [37] T.-F. Hung, Z.-W. Yin, S.B. Betzler, W. Zheng, J. Yang, H. Zheng, Nickel sulfide nanostructures prepared by laser irradiation for efficient electrocatalytic hydrogen evolution reaction and supercapacitors, *Chem. Eng. J.* 367 (2019) 115–122.
- [38] V. Londono-Calderón, R. Ospina, J. Rodriguez-Pereira, S.A. Rincón-Ortiz, E. Restrepo-Parra, Molybdenum and Nickel Nanoparticles Synthesis by Laser Ablation towards the Preparation of a Hydrodesulfurization Catalyst, *Catalysts* (2020).
- [39] T. Begildayeva, D. Chinnadurai, S.J. Lee, M.Y. Choi, Multifunctional photo-electrocatalysts of copper sulfides prepared via pulsed laser ablation in liquid: Phase formation kinetics and photo-electrocatalytic activity, *Int. J. Energy Res.* 46 (2022) 8201–8217.

[40] D. Chinnadurai, R. Rajendiran, P. Kandasamy, Bimetallic copper nickel sulfide electrocatalyst by one step chemical bath deposition for efficient and stable overall water splitting applications, *J. Colloid Interface Sci.* 606 (2022) 101–112.

[41] D. Chinnadurai, S.J. Lee, Y. Yu, S.Y. Nam, M.Y. Choi, Cation modulation in dual-phase nickel sulfide nanospheres by pulsed laser irradiation for overall water splitting and methanol oxidation reaction, *Fuel* 320 (2022) 123915.

[42] Y. Yu, S.J. Lee, J. Theerthagiri, Y. Lee, M.Y. Choi, Architecting the AuPt alloys for hydrazine oxidation as an anolyte in fuel cell: Comparative analysis of hydrazine splitting and water splitting for energy-saving H<sub>2</sub> generation, *Appl. Catal. B: Environ.* 316 (2022) 121603.

[43] S. Shankar Naik, J. Theerthagiri, F.S. Nogueira, S.J. Lee, A. Min, G.-A. Kim, G. Maia, L.M.C. Pinto, M.Y. Choi, Dual-Cation-Coordinated CoFe-Layered Double-Hydroxide Nanosheets Using the Pulsed Laser Ablation Technique for Efficient Electrochemical Water Splitting: Mechanistic Screening by In Situ/Operando Raman and Density Functional Theory Calculations, *ACS Catal.* 13 (2023) 1477–1491.

[44] T. Begildayeva, J. Theerthagiri, S.J. Lee, Y. Yu, M.Y. Choi, Unraveling the Synergy of Anion Modulation on Co Electrocatalysts by Pulsed Laser for Water Splitting: Intermediate Capturing by In Situ/Operando Raman Studies, *Small* (n/a) (2022) 2204309.

[45] J. Theerthagiri, K. Karuppasamy, A. Min, D. Govindarajan, M.L.A. Kumari, G. Muthusamy, S. Kheawhom, H.-S. Kim, M.Y. Choi, Unraveling the fundamentals of pulsed-laser-assisted synthesis of nanomaterials in liquids: Applications in energy and the environment, *Appl. Phys. Rev.* 9 (2022) 041314.

[46] S.J. Lee, J. Theerthagiri, M.Y. Choi, Time-Resolved Dynamics of Laser-Induced Cavitation Bubbles During Production of Ni Nanoparticles via Pulsed Laser Ablation in Different Solvents and Their Electrocatalytic Activity for Determination of Toxic Nitroaromatics, *Chem. Eng. J.* (2021) 130970.

[47] Y. Yu, S.Jun Lee, J. Theerthagiri, S. Fonseca, L.M.C. Pinto, G. Maia, M.Yong Choi, Reconciling of Experimental and Theoretical Insights on the Electroactive Behavior of C/Ni Nanoparticles with AuPt Alloys for Hydrogen Evolution Efficiency and Non-enzymatic Sensor, *Chem. Eng. J.* (2022) 134790.

[48] J. Theerthagiri, K. Karuppasamy, S.J. Lee, R. Shwetharan, H.-S. Kim, S.K.K. Pasha, M. Ashokkumar, M.Y. Choi, Fundamental and comprehensive insights on pulsed laser synthesis of advanced materials for diverse photo- and electrocatalytic applications, *Light: Sci. Appl.* 11 (2022) 250.

[49] Y. Oh, J. Theerthagiri, A. Min, C.J. Moon, Y. Yu, M.Y. Choi, Pulsed laser interference patterning of transition-metal carbides for stable alkaline water electrolysis kinetics, *Carbon Energy* (n/a) (2024) e448.

[50] Y. Oh, J. Theerthagiri, M.L. Aruna Kumar, A. Min, C.J. Moon, M.Y. Choi, Electrokinetic-mechanism of water and furfural oxidation on pulsed laser-interlaced Cu<sub>2</sub>O and CoO on nickel foam, *J. Energy Chem.* 91 (2024) 145–154.

[51] R.E. Haddad, S. Gazeau, J. Pécaut, J.-C. Marchon, C.J. Medforth, J.A. Shelnutt, Origin of the Red Shifts in the Optical Absorption Bands of Nonplanar Tetraalkylporphyrins, *J. Am. Chem. Soc.* 125 (2003) 1253–1268.

[52] B. Gera, A.K. Manna, P. Chandra Mondal, Metal-ions linked surface-confined molecular dyads of Zn-porphyrin–metallo-terpyridine: an experimental and theoretical study, *RSC Adv.* 7 (2017) 1290–1298.

[53] K. Ralphs, C. Zhang, S.L. James, Solventless mechanochemical metallation of porphyrins, *Green. Chem.* 19 (2017) 102–105.

[54] Z. Cheng, H. Abernathy, M. Liu, Raman Spectroscopy of Nickel Sulfide Ni<sub>3</sub>S<sub>2</sub>, *The. J. Phys. Chem. C.* 111 (2007) 17997–18000.

[55] C. Ouyang, X. Wang, C. Wang, X. Zhang, J. Wu, Z. Ma, S. Dou, S. Wang, Hierarchically Porous Ni<sub>3</sub>S<sub>2</sub> Nanorod Array Foam as Highly Efficient Electrocatalyst for Hydrogen Evolution Reaction and Oxygen Evolution Reaction, *Electrochim. Acta* 174 (2015) 297–301.

[56] W. He, H. Liu, J. Cheng, Y. Li, C. Liu, C. Chen, J. Zhao, H.L. Xin, Modulating the Electronic Structure of Nickel Sulfide Electrocatalysts by Chlorine Doping toward Highly Efficient Alkaline Hydrogen Evolution, *ACS Appl. Mater. Interfaces* 14 (2022) 6869–6875.

[57] M.R. Mollaeva, N. Yabbarov, M. Sokol, M. Chirkina, M.D. Mollaev, A. Zabolotskii, I. Seregina, M. Bolshov, A. Kaplin, E. Nikolskaya, Optimization, Characterization and Pharmacokinetic Study of Meso-Tetraphenylporphyrin Metal Complex-Loaded PLGA Nanoparticles, *Int. J. Mol. Sci.* 22 (2021) 12261.

[58] M.-S. Liao, S. Scheiner, Electronic structure and bonding in metal porphyrins, metal–Fe, Co, Ni, Cu, Zn, *J. Chem. Phys.* 117 (2002) 205–219.

[59] M. Aydin, DFT and Raman spectroscopy of porphyrin derivatives: Tetraphenylporphine (TPP), *Vib. Spectrosc.* 68 (2013) 141–152.

[60] N. Sonai Muthu, M. Gopalan, Polyethylene glycol-assisted growth of Ni<sub>3</sub>S<sub>4</sub> closely packed nanosheets on Ni-foam for enhanced supercapacitor device, *J. Solid State Electrochem.* 23 (2019) 2937–2950.

[61] R. Karthikeyan, D. Thangaraju, N. Prakash, Y. Hayakawa, Single-step synthesis and catalytic activity of structure-controlled nickel sulfide nanoparticles, *CrystEngComm* 17 (2015) 5431–5439.

[62] A. Gorski, A. Starukhin, S. Stavrov, S. Gawinkowski, J. Waluk, Resonance Raman spectroscopy study of protonated porphyrin, *Spectrochim. Acta Part A: Mol. Biomol. Spectrosc.* 173 (2017) 350–355.

[63] M.M. Makhlouf, Raman spectroscopy and optical constants of nanostructured oxovanadium(IV) tetraphenylporphyrin thin films, *Appl. Phys. A* 127 (2021) 368.

[64] E.V. Shah, V. Kumar, B.K. Sharma, K. Rajput, V.P. Chaudhary, D.R. Roy, Co-Tetraphenylporphyrin (co-TPP) in TM-TPP (TM = Fe, Co, Ni, Cu, and Zn) series: a new optical material under DFT, *J. Mol. Model.* 24 (2018) 239.

[65] H.M. Sturmeit, I. Cojocariu, A. Windischbacher, P. Puschning, C. Piamonteze, M. Jugovac, A. Sala, C. Africh, G. Comelli, A. Cossaro, A. Verdini, L. Floreano, M. Stredansky, E. Vesselli, C. Hohner, M. Kettner, J. Libuda, C.M. Schneider, G. Zamborlini, M. Cinchetti, V. Feyer, Room-Temperature On-Spin-Switching and Tuning in a Porphyrin-Based Multifunctional Interface, *Small* 17 (2021) 2104779.

[66] W.T. Figueiredo, G.B. Della Mea, M. Segala, D.L. Baptista, C. Escudero, V. Pérez-Dieste, F. Bernardi, Understanding the Strong Metal-Support Interaction (SMSI) Effect in CuxNi<sub>1-x</sub>/CeO<sub>2</sub> (0 < x < 1) Nanoparticles for Enhanced Catalysis, *ACS Appl. Nano Mater.* 2 (2019) 2559–2573.

[67] J. Kim, T. Begildayeva, J. Theerthagiri, C.J. Moon, A. Min, S.J. Lee, G.-A. Kim, M. Y. Choi, Manifolding active sites and *in situ*/operando electrochemical-Raman spectroscopic studies of single-metal nanoparticle-decorated CuO nanorods in furfural biomass valorization to H<sub>2</sub> and 2-furoic acid, *J. Energy Chem.* 84 (2023) 50–61.

[68] A. Li, S. Chen, F. Yang, H. Gao, C. Dong, G. Wang, Metalloporphyrin-Decorated Titanium Dioxide Nanosheets for Efficient Photocatalytic Carbon Dioxide Reduction, *Inorg. Chem.* 60 (2021) 18337–18346.

[69] P. Yin, Q.-Q. Yan, H.-W. Liang, Strong Metal-Support Interactions through Sulfur-Anchoring of Metal Catalysts on Carbon Supports, *Angew. Chem. Int. Ed.* 62 (2023) e202302819.

[70] N. Jiang, Q. Tang, M. Sheng, B. You, D.-e Jiang, Y. Sun, Nickel sulfides for electrocatalytic hydrogen evolution under alkaline conditions: a case study of crystalline NiS, NiS<sub>2</sub>, and Ni<sub>3</sub>S<sub>2</sub> nanoparticles, *Catal. Sci. Technol.* 6 (2016) 1077–1084.

[71] M.G.S. da Silva, C.M. Leite, M.A.L. Cordeiro, V.R. Mastelaro, E.R. Leite, One-Step Synthesis of Nickel Sulfides and Their Electrocatalytic Activities for Hydrogen Evolution Reaction: A Case Study of Crystalline h-NiS and o-Ni<sub>3</sub>S<sub>8</sub> Nanoparticles, *ACS Appl. Energy Mater.* 3 (2020) 9498–9503.

[72] K. Song, C. Tang, Z. Zou, Y. Wu, Modification of porous lignin with metalloporphyrin as an efficient catalyst for the synthesis of cyclic carbonates, *Transit. Met. Chem.* 45 (2020) 111–119.

[73] A. Mouradzadegun, S. Hamid, A. Sheikhzadeh, Takabi, Synthesis and characterization of porous organic polymer containing tailored AB<sub>3</sub> metalloporphyrin: highly active and reusable catalyst for oxidation of benzyl alcohol, *Res. Chem. Intermed.* 47 (2021) 4943–4955.

[74] M. Chen, X. Feng, L. Zhang, H. Ju, Q. Xu, J. Zhu, J.M. Gottfried, K. Ibrahim, H. Qian, J. Wang, Direct Synthesis of Nickel(II) Tetraphenylporphyrin and Its Interaction with a Au(111) Surface: A Comprehensive Study, *J. Phys. Chem. C.* 114 (2010) 9908–9916.

[75] J. Park, H. Lee, Y.E. Bae, K.C. Park, H. Ji, N.C. Jeong, M.H. Lee, O.J. Kwon, C. Y. Lee, Dual-Functional Electrocatalyst Derived from Iron-Porphyrin-Encapsulated Metal–Organic Frameworks, *ACS Appl. Mater. Interfaces* 9 (2017) 28758–28765.

[76] Y. Sun, J. Wu, Z. Zhang, Q. Liao, S. Zhang, X. Wang, Y. Xie, K. Ma, Z. Kang, Y. Zhang, Phase reconfiguration of multivalent nickel sulfides in hydrogen evolution, *Energy Environ. Sci.* 15 (2022) 633–644.

[77] C. Lan, H. Xie, Y. Wu, B. Chen, T. Liu, Nanoengineered, Mo-Doped, Ni<sub>3</sub>S<sub>2</sub> Electrocatalyst with Increased Ni–S Coordination for Oxygen Evolution in Alkaline Seawater, *Energy Fuels* 36 (2022) 2910–2917.

[78] A. Mondal, A. Vomiero, 2D Transition Metal Dichalcogenides-Based Electrocatalysts for Hydrogen Evolution Reaction, *Adv. Funct. Mater.* 32 (2022) 2208994.

[79] S. Naik Shreyanka, J. Theerthagiri, S.J. Lee, Y. Yu, M.Y. Choi, Multiscale design of 3D metal–organic frameworks (M–BTC, M: Cu, Co, Ni) via PLAL enabling bifunctional electrocatalysts for robust overall water splitting, *Chem. Eng. J.* 446 (2022) 137045.

[80] Q. Cao, S. Hao, Y. Wu, K. Pei, W. You, R. Che, Interfacial charge redistribution in interconnected network of Ni<sub>2</sub>P–Co<sub>2</sub>P boosting electrocatalytic hydrogen evolution in both acidic and alkaline conditions, *Chem. Eng. J.* 424 (2021) 130444.

[81] L. Kuai, J. Geng, C. Chen, E. Kan, Y. Liu, Q. Wang, B. Geng, A Reliable Aerosol-Spray-Assisted Approach to Produce and Optimize Amorphous Metal Oxide Catalysts for Electrochemical Water Splitting, *Angew. Chem. Int. Ed.* 53 (2014) 7547–7551.

[82] L. Luo, Z.-j. Wang, X. Xiang, D. Yan, J. Ye, Selective Activation of Benzyl Alcohol Coupled with Photoelectrochemical Water Oxidation via a Radical Relay Strategy, *ACS Catal.* 10 (2020) 4906–4913.

[83] D. Xie, S. Li, W. Yang, S. Fan, Y.-S. Feng, Selective Photocatalytic Conversion of Benzyl Alcohol to Benzaldehyde by Antimony(V) Porphyrin Metal–Organic Frameworks under Visible-Light Irradiation, *ChemistrySelect* 7 (2022) e202103521.

[84] F. Adam, W.-T. Ooi, Selective oxidation of benzyl alcohol to benzaldehyde over Co-metallocporphyrin supported on silica nanoparticles, *Appl. Catal. A: Gen.* 445–446 (2012) 252–260.

[85] R. Li, P. Kuang, L. Wang, H. Tang, J. Yu, Engineering 2D NiO/Ni<sub>3</sub>S<sub>2</sub> heterointerface electrocatalyst for highly efficient hydrogen production coupled with benzyl alcohol oxidation, *Chem. Eng. J.* 431 (2022) 134137.

[86] J. Li, X. Tian, X. Wang, T. Zhang, M.C. Spadaro, J. Arbiol, L. Li, Y. Zuo, A. Cabot, Electrochemical Conversion of Alcohols into Acidic Commodities on Nickel Sulfide Nanoparticles, *Inorg. Chem.* 61 (2022) 13433–13441.

[87] J. Zhang, C. Xu, D. Zhang, J. Zhao, S. Zheng, H. Su, F. Wei, B. Yuan, C. Fernandez, Facile Synthesis of a Nickel Sulfide (NiS) Hierarchical Flower for the Electrochemical Oxidation of H<sub>2</sub>O<sub>2</sub> and the Methanol Oxidation Reaction (MOR), *J. Electrochim. Soc.* 164 (2017) B92.

[88] H. Li, L. Cao, C. Yang, Z. Zhang, B. Zhang, K. Deng, Selective oxidation of benzyl alcohols to benzoic acid catalyzed by eco-friendly cobalt thioporphyrazine catalyst supported on silica-coated magnetic nanospheres, *J. Environ. Sci.* 60 (2017) 84–90.

[89] C. Fabbri, C. Aurisicchio, O. Lanzalunga, Iron porphyrins-catalysed oxidation of  $\alpha$ -alkyl substituted mono and dimethoxylated benzyl alcohols, *Cent. Eur. J. Chem.* 6 (2008) 145–153.

[90] L. Wei, M.D. Hossain, M.J. Boyd, J. Aviles-Acosta, M.E. Kreider, A.C. Nielander, M. B. Stevens, T.F. Jaramillo, M. Bajdich, C. Hahn, Insights into Active Sites and Mechanisms of Benzyl Alcohol Oxidation on Nickel–Iron Oxyhydroxide Electrodes, *ACS, Catalysis* 13 (2023) 4272–4282.

[91] Y. Zhu, T.-R. Kuo, Y.-H. Li, M.-Y. Qi, G. Chen, J. Wang, Y.-J. Xu, H.M. Chen, Emerging dynamic structure of electrocatalysts unveiled by *in situ* X-ray diffraction/absorption spectroscopy, *Energy Environ. Sci.* 14 (2021) 1928–1958.

[92] J. Wang, H.-Y. Tan, M.-Y. Qi, J.-Y. Li, Z.-R. Tang, N.-T. Suen, Y.-J. Xu, H.M. Chen, Spatially and temporally understanding dynamic solid–electrolyte interfaces in carbon dioxide electroreduction, *Chem. Soc. Rev.* 52 (2023) 5013–5050.